

Contents lists available at [ScienceDirect](https://www.sciencedirect.com)

# Journal of Wind Engineering & Industrial Aerodynamics

journal homepage: [www.elsevier.com/locate/jweia](http://www.elsevier.com/locate/jweia)

## A field study on the aerodynamics of freight trains with different stacking configurations

Ariq Quazi <sup>a,\*</sup>, Timothy Crouch <sup>a</sup>, James Bell <sup>a,c</sup>, Tony McGreevy <sup>b</sup>, Mark C. Thompson <sup>a</sup>, David Burton <sup>a</sup>

<sup>a</sup> Department of Mechanical and Aerospace Engineering, Monash University, PO Box 31, 3800, Australia

<sup>b</sup> Pacific National, Melbourne, Victoria, Australia

<sup>c</sup> German Aerospace Center (DLR), Institute for Aerodynamics and Flow Technology (AS), Göttingen, Germany

### ARTICLE INFO

#### Keywords:

Train Aerodynamics  
Freight  
Field Experiment  
Pressure Drag  
Correlation  
Full-scale

### ABSTRACT

A full-scale 48-foot shipping container was instrumented with surface pressure taps and loaded onto a number of single- and double-stacked container freight trains. Surface pressure data enabled the container pressure drag coefficient to be evaluated for a range of different train loading configurations, container positions along the train, and atmospheric wind conditions. Field-based measurements show that for low and high crosswind conditions surface pressure distributions measured on the front face of the instrumented container are in good agreement with those reported in past studies. However, the magnitude of the pressure drag coefficient was found to be typically 50% lower for all loading cases analysed compared with previous seemingly analogous wind-tunnel and numerical investigations. For high crosswind conditions, the drag coefficient was found to increase and correlated well with the level of asymmetry observed in the measured pressure distributions. This was true for all cases regardless of the position along the length of the train. In the absence of direct information of the incident free-stream wind conditions, the level of asymmetry in the pressure distributions was found to provide a viable indirect method for assessing the impact that crosswinds have on the aerodynamic drag of freight trains.

### 1. Introduction

Intermodal freight trains are a critical and favoured transport method for a variety of freight types due to their high capacity, modular capability and overall efficiency. In essence, intermodal freight trains consist of a set of flat wagons on which shipping containers containing freight are loaded. However, this modularity means that no two loaded trains are the same, posing a challenge for rail operators to find means of optimising fuel consumption. By better understanding the different types of resistances that must be overcome, targeted improvements can be implemented. A key resistance that is often not considered is the aerodynamics of the train. Often mass distribution and scheduling optimisation are seen as primary avenues of improvement (Lai and Barkan, 2005; Lai et al., 2008). However, with the aerodynamic drag increasing exponentially with train speed (Davis, 1926), and where speeds in excess of 100 km/h are commonly seen, an opportunity exists to optimise the stacking configurations of containers to reduce the overall pressure drag experienced by the train.

Different container geometries, wagon types, container arrangements and either single- or double-stacking result in the flow over an

individual train varying considerably. Coupled with varying effective gap spacing between containers and the extreme length of a train, a lab-based analysis for a particular train in the field poses a difficult task. As such, it is common for wind-tunnel and numerically based studies to make a number of assumptions and simplifications to gain a better understanding of the effect of a particular parameter in a controlled environment (Gielow and Furlong, 1988; Watkins et al., 1992; Soper et al., 2014; Li et al., 2017; Maleki et al., 2019).

This work follows on from the initial study of Quazi et al. (2020), where a methodology for assessing the pressure drag of a container on board an operational full-scale train was presented. The focus of that work was the characterisation of drag on a representative container and the dependence of drag on crosswind. It also provided a detailed assessment of measurement uncertainties and correlation with wind speed and direction data obtained from weather stations close to the route. The current work builds upon the study, using the same test set-up, to investigate the effect of container position and gap spacing for a number of different local loading configurations. It provides important

\* Corresponding author.

E-mail address: [ariq.quazi@monash.edu](mailto:ariq.quazi@monash.edu) (A. Quazi).

<https://doi.org/10.1016/j.jweia.2022.105245>

Received 18 July 2022; Received in revised form 28 October 2022; Accepted 14 November 2022

Available online 2 December 2022

0167-6105/© 2022 Elsevier Ltd. All rights reserved.

new field data on the pressure distributions on container trains, which has been accumulated over many journeys of significant length.

### 1.1. Gap spacing

The nature of the operation of many intermodal freight train trips is that gaps between sequential containers are inevitable. The ideal loading configuration of a freight train would be to have minimal gap spacings hence allowing the boundary layer to remain essentially attached over the entire length of the train. However, gaps may be required for operational reasons, such as having to move a certain number of wagons from one city to another or a set of wagons being grouped together and a certain container not being able to fit. Slot utilisation is often a parameter used to determine how many slots are used on a given train, however, the positions of certain gap sizes are generally not accounted for. Lai et al. (2008) attempted to address this by defining a slot efficiency parameter based on an exponential model from the work of Engdahl et al. (1987) and Gielow and Furlong (1988) for each gap, and found that optimising the gap spacing for a sample route resulted in a saving of 56 million litres of fuel per year. As such, understanding how and where to position the gaps provides an opportunity to reduce the resistive pressure drag force experienced by each container and the overall aerodynamic drag on the train.

The flow around an isolated container in freestream has been well understood given the fundamental bluff-body shape of a shipping container is equivalent to an elongated rectangular prism. The oncoming flow impinges on the front surface creating a region of high pressure. As the flow accelerates towards the side and roof windward edges, the shear layer separates, resulting in a region of low pressure immediately downstream of the edges. The separated flow then reattaches over the length of the container. This flow state was shown by Taylor et al. (2011) for a two-dimensional elongated bluff body with a length-to-height ratio of 7:1, and later by Östh and Krajnović (2014) for a three-dimensional representative wagon and container with a length to width ratio of 5:1. Further, Li et al. (2015) and Maleki et al. (2017) concluded through wind-tunnel tests and numerical simulations, respectively, that similar features were evident for a double-stacked configuration, where the aspect ratio of the frontal area was 2:1.

On the base surface, two asymmetric time-mean separation regions in the spanwise plane have been observed, with the core of the lower vortex closer to the face of the container (Östh and Krajnović, 2014; Uystepruyst and Krajnović, 2013; Maleki et al., 2019; Quazi et al., 2020). This is caused by the air losing momentum as it interacts with the detailed wagon features below the container. The core of the higher vortex was seen to be further downstream due to the higher flow velocity over the top of the container. A time-mean ring vortex is also observed, which is formed by the rolling up of the four separating shear layers off the trailing edges combining together.

The effect of multiple successive containers with various gap sizes for a double-stacked train has been well studied by Maleki et al. (2019) and Li et al. (2017). It was shown that the pressure on the front of the container had an overwhelmingly dominant effect on the drag coefficient. The pressure drag was seen to increase up to a gap size of  $9.46W$  (normalised by the width ( $W$ ) of the container) in the wind-tunnel study of Li et al. (2017) and up to  $5.76W$  in the numerical simulation of Maleki et al. (2019). For gap sizes larger than this the drag remained constant. The highest rate of change was seen between  $1.77W$  and  $3.23W$ , and this was explained to be due to the wake of the upstream container closing behind the body allowing the freestream flow to enter the gap and to impinge on the front face of the downstream container. The effect of an entire empty slot being present for a single-stacked container was investigated by Gielow and Furlong (1988). They found the difference in the drag coefficient on a container with and without an upstream empty slot to be 0.175.

### 1.2. Position along train

Intermodal freight trains can often be in excess of 1.5 km in length, posing an almost impossible challenge to test a full-length model in a wind-tunnel or even through numerical simulation (Bell et al., 2020). The practical limiting factor in a wind-tunnel is the small scale required to fit an entire model, resulting in the floor boundary layer engulfing the model if mounted to the floor and an extreme reduction in the Reynolds number. For numerical modelling, computing time and memory requirements become prohibitive given the size and resolution requirements of a representative model. Modelling approaches such as employing streamwise periodic boundary conditions can partially account for these challenges as shown by Östh and Krajnović (2014), where it was found that drag associated with the 'middle' portion of the train was 90% lower than the leading locomotive. However, it implies a constant boundary-layer thickness along the entire length of the train. To address this assumption in the recent work of Maleki (2020), a repeated arrangement of two different computation domains modelling a single gap ( $6.46W$ ) every second domain was implemented where the second domain has no gaps. This allows the boundary layer to relax and reduced the possibility of the upstream influence in the flow of the test wagon in the repeated domain downstream. The outlet parameters are then saved and used as the inlet parameter for the next iteration. It was shown that after the eighth test wagon the drag stabilised, however, the boundary layer thickness kept increasing. This was similar to Soper and Baker (2020) who also found the boundary layer to keep growing during full-scale track side slipstream tests.

Indeed, most scale models make the assumption that after a certain distance from the front of the train the drag for a given gap size no longer changes, hence that value is representative for the majority of the length of the train Watkins et al. (1992), Engdahl et al. (1987), Golovanevskiy et al. (2012). This assumption may have merit since it has been shown that the slipstream boundary layer stops increasing in width away from the sides of the train after a certain distance from the front. This is in contrast to that of Maleki (2020) and Soper and Baker (2020). However, in Soper and Baker (2020), who investigated different passenger and freight train types suggests this could be function of the particular train type. Soper et al. (2014) found the slipstream stabilisation distance to be around 100 m based on moving model experiments, whereas Bell et al. (2020) estimated this length to be at around 200 m through full-scale field testing. Note, the influence of crosswinds on this length has not been understood. Further, for more irregular stacking types where there are larger gap sizes, the boundary layer may no longer remain attached as freestream flow enters the gap. Bell et al. (2020) found that a combination of multiple gaps ( $< 2$  m, or  $0.69W$ ) had a more significant effect on the boundary layer as opposed to one large gap. As such this creates a need to undertake further full-scale testing where the influence of such parameters can be tested and hence this forms the motivation for the current study.

### 1.3. Crosswinds

Flynn et al. (2016) and Soper et al. (2015) undertook numerical and moving model experiments on the same test set-up as Soper et al. (2014), investigating the effect of  $30^\circ$  wind yaw angles over a range of gap sizes for a single-stacked 4-wagon consist. Findings similar to those in Maleki et al. (2020) were found, however, given the larger yaw angle analysed the base pressure was characterised by a region of negative pressure where a smaller gap size resulted in a large degree of asymmetry in the pressure distribution. This was explained to be due to the flow accelerating through the smaller gap. For larger gap sizes the distribution was seen to be relatively uniform. Studies by Beagles and Fletcher (2013), Giappino et al. (2018), Golovanevskiy et al. (2012), who only investigated the pressure drag coefficient, observed that a quadratic trend with yaw angle exists up to  $30^\circ$  after which the drag starts to decrease. Further to this, the effect of crosswinds can also



Fig. 1. Instrumented 48-foot (14.6 m) refrigeration shipping container (white) on-board an operational freight train with significantly flatter external ridges than conventional containers (green). (For interpretation of the references to colour in this figure legend, the reader is referred to the web version of this article.)

drastically change the slipstream boundary layer. Bell et al. (2020) found that wind yaw angles as small as two degrees completely disrupt the slipstream boundary layer with low pressures being observed on the leeward side of the train.

Maleki et al. (2020) has shown through numerical simulation the flow physics governing the aerodynamics of yawed flow conditions for the double-stacked train for multiple upstream gap sizes. The highest rate of change in drag coefficient for yaw angles  $\leq 5$  deg occurs between  $1.77W - 3.23W$ . This was also observed by Li et al. (2017) for zero-yaw conditions, which suggests that the majority of the freestream flow remains attached. This is due to two counter-rotating vortices enclosing the wake of the container and shielding the gap from the freestream flow even at small yaw angles. For yaw angles  $\geq 10$  deg the highest rate of change in gap flow is determined to lie between  $0.3W$  and  $1.77W$ . This is due an unsteady longitudinal vortex forming off the top windward corner of the upstream container and propagating downstream along the leeward and top faces creating regions of low pressure. This prevents the wake behind the container to fully close, hence allowing the entrainment of the freestream flow into the gap to impinge on the front face. At larger front gap sizes, e.g.,  $6.46W$ , the same effect is seen, however, there is a greater asymmetric pressure distribution. Changing the base gap size was seen to have minimal effect with the dominating contribution coming from the changes in the front gap size only.

#### 1.4. Aim of this study

Relevant field measurements for various models have been successful in the past validating laboratory- and numerical-based studies. For example, Surry (1991) and Richardson et al. (1997) investigated the pressures on a full-scale building and Quinn et al. (2007) conducted experiments of a commercial full-scale vehicle analysing the induced rolling moment. Similarly, field data has also been obtained for an operational freight train such as in the work of Sterling et al. (2008), Bell et al. (2020) and Soper and Baker (2020) who investigated the slipstream boundary layer. On board force and pressure results have also been provided by Engdahl et al. (1987) and Gallagher et al. (2018), however, these have mostly been of a limited resolution. More recently Bell et al. (2022) instrumented a container in a similar manner to the current study, with the inclusion of LiDAR sensors and thermal cameras to characterise the surrounding topology. As such the current set up (Quazi et al., 2020) is the first of its kind known to the authors whereby a full-scale shipping container was pressure-tapped on either end and could be placed anywhere along the length of the train.

Hence, the aim of this study is to obtain and interpret field measurements, correlating results to those from past wind-tunnel and numerical simulations. In particular, the effects of the gap spacing, stacking type, and position along the train are investigated. In addition, the effect of these variables under varying wind conditions is also considered. This work is in collaboration with Pacific National – a freight transport

provider within Australia – with the ultimate goal of reducing the fuel consumption of freight trains by optimising the loading of different freight types to improve the aerodynamics, thereby reducing fuel costs and greenhouse gas emissions. To this end practical outcomes and stacking considerations are also provided following an estimation of the aerodynamic efficiency of various configurations. Finally, we aim to add important reference data to the limited field measurements available on freight train aerodynamics.

## 2. Methodology

This section describes the Data Acquisition System (DAS), the different container loading configurations and the transcontinental route taken by the container. A detailed description of the DAS and instrumented container can be found in Quazi et al. (2020) along with the uncertainties associated with the acquired data.

### 2.1. Instrumented container & data acquisition system

A 48-foot refrigeration container with dimensions of 13.50 m (length), 2.44 m (width) and 2.90 m (height) was instrumented with an on-board DAS and pressure tapped on either end of the container. The particular container class selected was due its comparatively smoother outer geometry than other container variants, as can be seen in Fig. 1 when compared to a standard container. Also importantly, this provided a better comparison with the more simplified generic geometries typically employed in experimental and numerical studies (Li et al., 2017, Maleki et al., 2017).

Fig. 2 depicts the array of 59 pressure taps on the front and base faces of the container. The taps were evenly distributed over the faces apart from the edges where the density of the taps was increased to better resolve expected high-pressure gradients. The differential pressure was measured with respect to a plenum inside the instrumentation box, with two reference pressure tubes located free inside the container. An on-board Global Positioning System (GPS) provided the train velocity, altitude and position information throughout the route. Also on-board was a PC that logged all the data and all instrumentation was run off four 12-volt absorbed glass-gel mat batteries. Surface pressure data was logged over particular track sections at a frequency of 1 Hz. A rolling 60 s time-average filter was applied to the data set. Findings presented in this study are a result of excluding data that was measured when the train ground speed was below 60 km/h.

### 2.2. Test track and loading configurations

Fig. 3 illustrates the transcontinental journey taken by the container between Australian cities Melbourne and Perth stopping via Adelaide and returning via the same route. The duration of the journey between Melbourne and Adelaide was approximately 9 h (~830 km) and almost 37 h between Adelaide the Perth (~2500 km). In order to optimise the

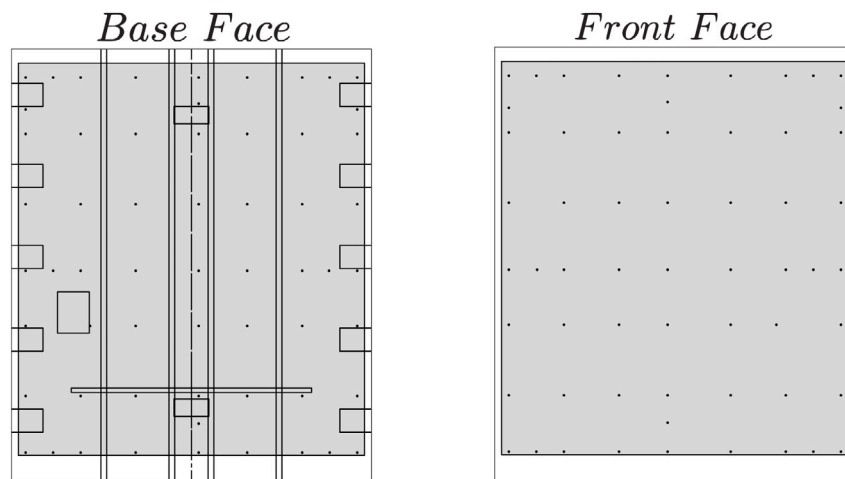


Fig. 2. Array of pressure taps on the front and base face where the shaded area represents the region over which pressure distributions have been interpolated. The final pressure distribution was extrapolated to the outer edges of the container.

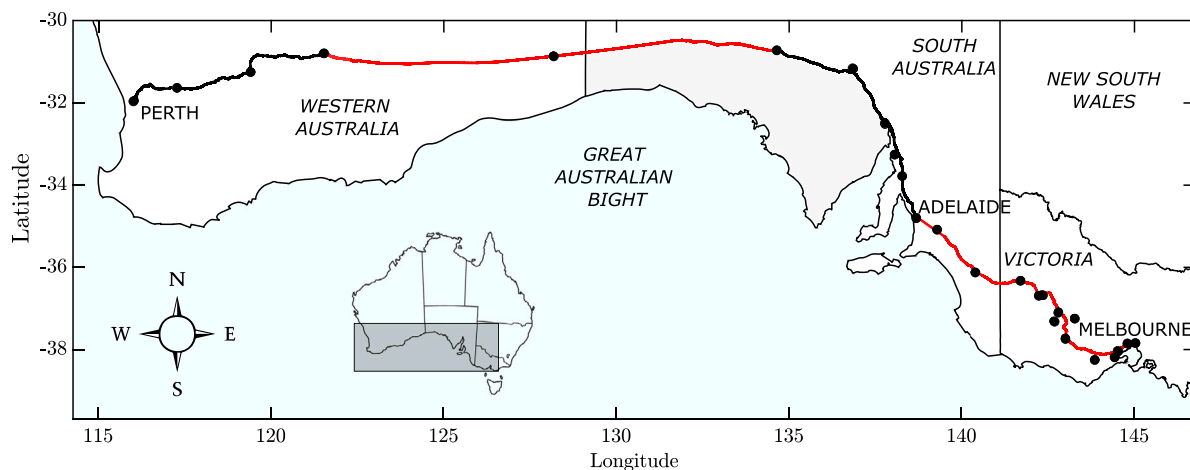


Fig. 3. Transcontinental path taken by freight trains across Australia between the cities of Melbourne, Adelaide, and Perth. Red sections indicate portions of the journey where data was continuously recorded. The bullet (•) markers are BoM weather stations. (For interpretation of the references to colour in this figure legend, the reader is referred to the web version of this article.)

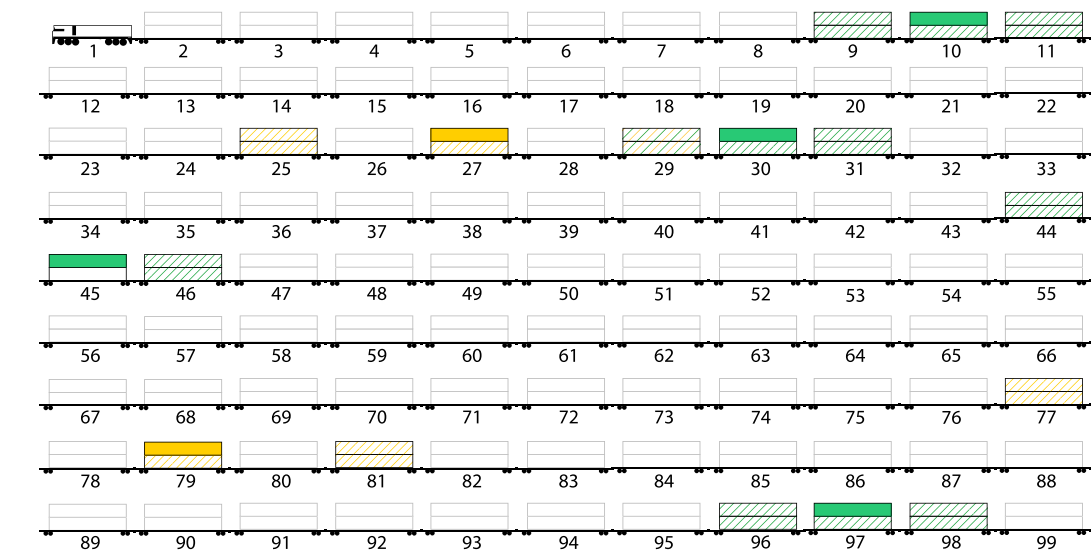
on-board battery consumption given the extensive distances involved, only portions of the entire journey were continuously logged, highlighted in red in Fig. 3. Portions that were not logged included hilly terrain where the average velocity was low or varied significantly. In addition, the start and end of the sections coincided with Bureau of Meteorology (BoM) weather stations.

The container was unloaded at each capital city and loaded back onto another train in a different loading configuration. This resulted in a total of 15 different loading configurations, 5 double-stacked, and 9 single-stacked. Unfortunately, due to operational constraints, the authors had only limited input into the test container position and overall train configuration. Fig. 4 depicts the local stacking configurations, which are characterised by (i) whether the container is single or double-stacked, (ii) the local gap size on either side of the instrumented container, and (iii) the position of the container along the length of the train. For all double-stacked configurations the container was positioned on the top, since half of the bottom container was inside the well-type wagon which would make it difficult to compare to simplified geometry results used in past wind-tunnel and numerical studies (Li et al., 2017, Maleki et al., 2017). The length of each train varied between 0.55 and 1.70 km, with the closest container position to the front of the train being 0.17 km and the furthest being at

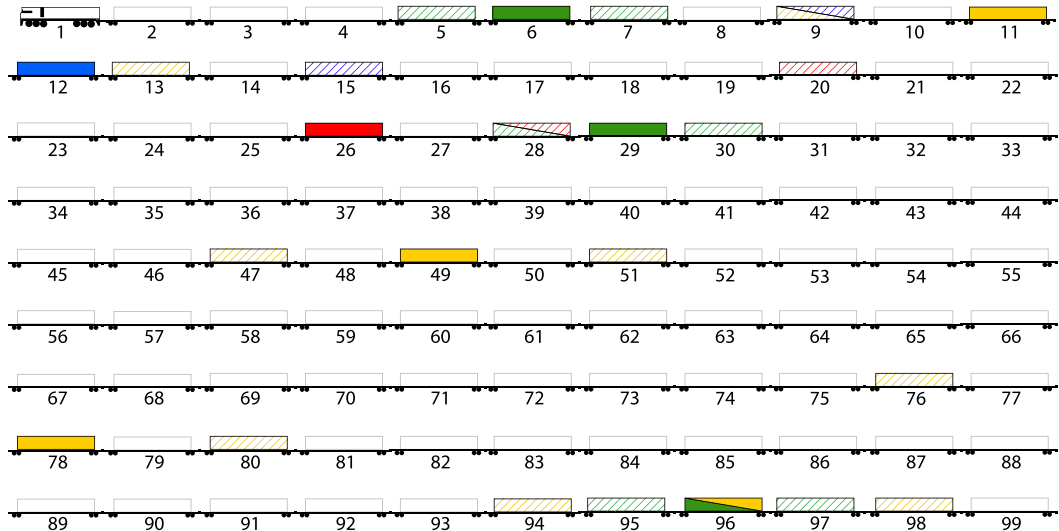
1.47 km. Gap sizes normalised by the width of the container varied between  $0.3W$  and  $56.9W$  for single-stacked configurations and  $1.8W$  and  $11.4W$  for double-stacked configurations. Table 1 summarises the cities bounding each trip and the relevant configurations details. Fig. 3 also highlights a number of BoM weather stations that were identified along the track.

### 2.3. Weather conditions

Weather conditions during the trip were determined by acquiring data from BoM weather stations. The acquired data consisted of local temperature, mean sea pressure level (MSPL), relative humidity, wind speed, and wind direction at one-minute intervals. The density for the drag coefficient was corrected based on the MSPL and altitude, where the altitude varied from 10 m to 685 m from sea level. Given the sparse distribution of the weather stations only the station closest to the train at a given time was used. An interpolation method between stations was attempted but given their local dependency it did not yield reliable results. Only the average weather conditions were of interest hence the 1 min data was averaged over 30 min intervals to smooth the data. A summary of the weather conditions for different trips can be seen in Tables 2 and 3. The average train speed ( $\bar{V}_T$ ), relative velocity ( $\bar{V}_r$ ),



(a) double-stacked gap sizes. ■ : 1.75W - 3.37W, ■ : 11.43W - 12.10W



(b) single-stacked gap sizes. ■ : 0.26W - 0.76W, ■ : 4.97W - 6.87W, ■ : 13.57W, ■ : 21.88W

Fig. 4. (a) Double and (b) single-stacked configurations that were tested. Note that only the local loading configuration either side of the instrumented container is shown. In all cases, the front and base gap size were the same. Solid colours represent the position of the instrumented container with hatched colouring representing the local containers either side. Diagonally divided containers are containers in the same position but for a different loading arrangement. (For interpretation of the references to colour in this figure legend, the reader is referred to the web version of this article.)

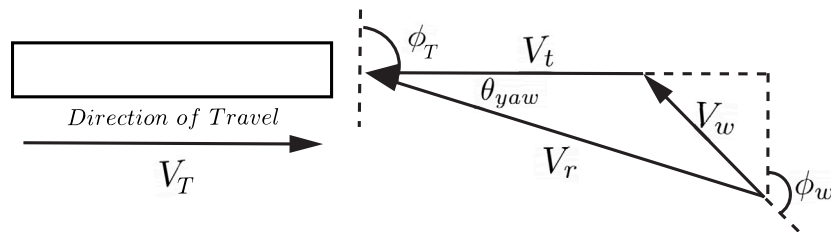


Fig. 5. Velocity vector diagram and definitions. Here,  $\phi_w$  is the wind direction from which it is originating, and  $\phi_T$  is the heading direction of the train both measured relative to True north.  $V_t$  is the train velocity seen by the wind which is equal and opposite to the real train velocity,  $V_T$ .

and yaw angle ( $\bar{\theta}_{yaw}$ ), were only considered when the train velocity was over 60 km/h. Of note is that the wind direction ( $\bar{\phi}_w$ ) is given from the direction in which the wind originates whereas the heading direction ( $\bar{\phi}_T$ ) is the direction in which train is actually heading towards. This enabled the wind type to be determined to be either a tail, head, or

crosswind. Fig. 5 defines the convention used to determine the relative train velocity and yaw angle. The results were then compared to the observed pressures on the container to explain the differences seen in the drag coefficient and the distribution.

**Table 1**

Summary of gap sizes and positions along train for all trips. The results of a select few have been discussed herein and have been given a corresponding ID. This is due to the remaining runs either having a stacking configuration dominated by local discrepancies or other technical difficulties. All trips have been included to provide an idea of the scope of the test program.

Trip number	ID	Departing city	Arriving city	Upstream gap ( $G_f/W$ )	Downstream gap ( $G_b/W$ )	Position along train (km)
Trip 1	–	Melbourne	Adelaide	0.76	0.26	0.17
Trip 2	S4(0)	Melbourne	Adelaide	0.31	0.31	0.43
Trip 3	–	Melbourne	Adelaide	0.26	0.26	0.19
	S5(0)	Adelaide	Melbourne	0.31	0.26	0.08
Trip 4	–	Melbourne	Adelaide	1.63	19.40	0.73
	–	Adelaide	Perth	10.45	10.45	0.76
	S1(1)	Perth	Adelaide	7.02	7.02	1.14
Trip 5	S2(1)	Melbourne	Adelaide	6.74	7.02	0.72
	–	Adelaide	Perth	2.79	2.79	0.70
	D1(0)	Perth	Adelaide	2.79	2.79	1.41
	S7(2+)	Adelaide	Melbourne	13.57	12.91	0.19
Trip 6	S3(1)	Melbourne	Adelaide	6.87	7.02	1.40
	D4(1)	Adelaide	Perth	10.45	10.45	1.16
	D2(0)	Perth	Adelaide	2.79	2.79	0.14
	S6(0)	Adelaide	Melbourne	0.31	0.76	1.40
Trip 7	S8(2+)	Melbourne	Adelaide	56.38	12.91	1.34
	–	Adelaide	Perth	2.79	2.79	1.04
	D3(0)	Perth	Adelaide	2.79	2.79	0.44
Trip 8	–	Melbourne	Adelaide	21.88	9.52	0.48
	D5(1)	Adelaide	Perth	10.45	10.45	0.39
	–	Perth	Adelaide	1.75	1.75	0.65
	–	Adelaide	Melbourne	3.20	3.20	0.08

**Table 2**

Summary of general wind conditions for double-stacked configuration (denoted as D1, D2, D3...) over the length of the trip. The bracketed numbers after the title represent the number of 40 ft empty slots either side of the instrumented container. Where,  $\bar{T}$  is average temperature,  $\bar{V}_w$  is the wind velocity,  $\bar{V}_T$  is the train velocity,  $\bar{V}_r$  is the relative train velocity and  $\bar{\theta}_{yaw}$  is the wind yaw angle.

Parameter	Run D1(0)	Run D2(0)	Run D3(0)	Run D4(1)	Run D5(1)
$\bar{T}$ (°C)	21.6	22.3	14.1	27.6	18.1
$\bar{V}_w$ (km/h) and $\bar{\phi}_w$ (°)	16.7 ESE	14.9 ESE	12.8 S	20.7 S	17.6 SW
$\bar{V}_T$ (km/h) and $\bar{\phi}_T$ (°)	88.2 E	94.0 E	87.2 E	89.5 W	96.7 W
$\bar{V}_r$ (km/h)	76.1	90.7	85.5	84.1	92.1
Identified wind type	Head	Head	Cross	Cross	Head
$\bar{\theta}_{yaw}$ (°)	–2.5	3.1	–6.1	–7.4	–6.7

**Table 3**

Summary of general wind conditions for single-stacked configurations (denoted as S1, S2, S3...) over the length of the trip. The bracketed numbers after the title represent the number of empty slots either side of the instrumented container.

Parameter	Run S1(1)	Run S2(1)	Run S3(1)	Run S4(0)	Run S5(0)	Run S6(0)	Run S7(2+)	Run S8(2+)
$\bar{T}$ (°C)	21.7	14.0	11.7	6.1	8.6	21.0	18.9	8.0
$\bar{V}_w$ (km/h) and $\bar{\phi}_w$ (°)	30.4 SW	11.5 SSW	5.0 SE	15.2 W	9.2 SSW	34.7 NW	9.3 ENE	9.1 NW
$\bar{V}_T$ (km/h) and $\bar{\phi}_T$ (°)	91.5 E	91.2 WNW	85.2 WNW	89.3 W	89.8 ESE	89.7 SE	83.3 ESE	91.8 WNW
$\bar{V}_r$ (km/h)	110.7	95.6	87.1	86.9	90.0	117.2	81.6	86.8
Identified wind type	Tail	Cross	Tail	Head	Cross	Tail	Head	Head
$\bar{\theta}_{yaw}$ (°)	–13.1	3.1	–1.1	1.9	–4.4	2.6	3.1	1.5

### 3. Results and discussion

In the following section, the time-averaged results relating to the effect of gap spacing, loading type and container position along the length of the train are discussed. Varying natural wind conditions are experienced throughout the trip, and as such, low and high crosswind cases are also characterised and analysed. These results are compared to previous numerical and experimental results to establish similarities.

The pressure drag coefficient, throughout the analysis is defined as

$$C_D = \frac{\bar{P}_{front} - \bar{P}_{base}}{1/2 \cdot \rho \cdot V_t^2}, \quad (1)$$

where  $C_D$  is the difference in the area-averaged front pressure,  $\bar{P}_{front}$ , and the base pressure,  $\bar{P}_{base}$ , represented as a force coefficient,  $\rho$  is the air density and  $V_t$  is the train velocity seen by the wind. The air density was corrected for altitude. Fig. 6 illustrates the velocity and altitude

time series for an example trip between Adelaide and Perth, Australia. The highlighted section, shown in red, corresponds to that shown in Fig. 3. This section of track was selected to be logged for all trips, as it had long stretches of flat and straight tracks across the Nullabor region, where the velocity of the train maintained its maximum speed for extended periods of time. The final consideration into selecting this section was to optimise the battery usage and only log sections over which reliable data would be obtained, as it is evident that outside this section the velocity fluctuates more significantly. Further details regarding the time-average analysis carried out for each trip can be found in Quazi et al. (2020).

#### 3.1. Effect of gap spacing

Due to freight and logistic regulations, it was not possible to mount sensor equipment on the locomotive or on the outside surface of the

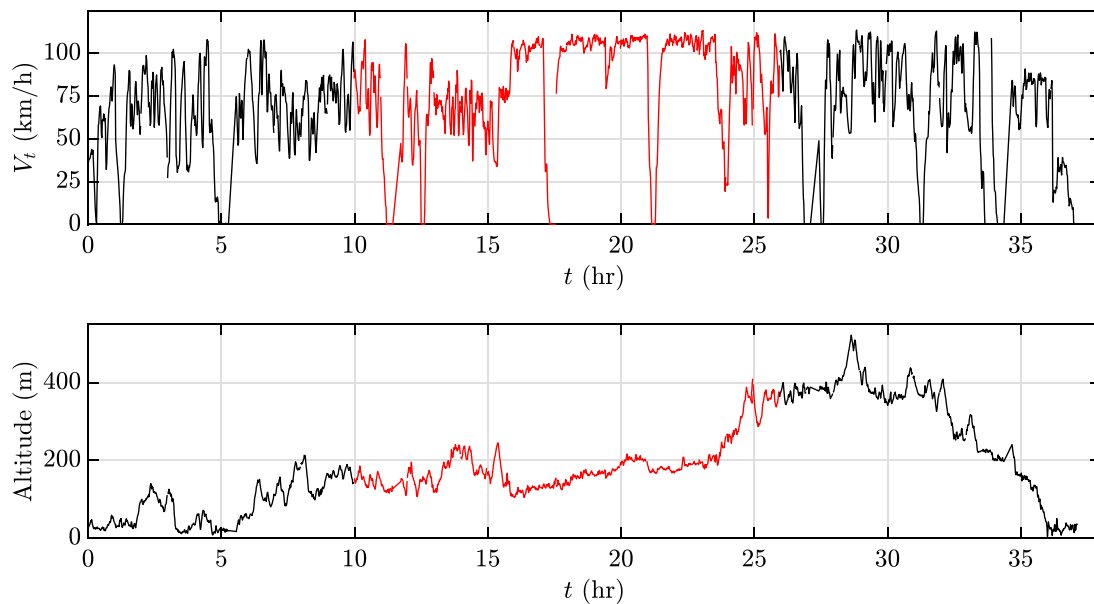


Fig. 6. Time series of velocity (top) and altitude (bottom) of one trip from Adelaide to Perth. Highlighted section (red) is where data was obtained over multiple trips. (For interpretation of the references to colour in this figure legend, the reader is referred to the web version of this article.)

container to measure wind speed or direction directly. However, Quazi et al. (2020) demonstrated that a relationship exists between the degree of symmetry of the left and right halves of the front surface pressure distribution and the gap sensitive (front) surface pressure coefficient characterised by an ‘asymmetry measure’,

$$C_{P_a} = C_{P_{front, left}} - C_{P_{front, right}} \quad (2)$$

It was also determined that the asymmetry measure correlated with the observed wind conditions providing a proxy to estimate the wind yaw angle. This was initially carried out for one trip where the container was single-stacked with a gap size of  $13.4W$  (normalised by the container width) either side the instrumented container (Quazi et al., 2020). It was suggested that for a  $C_{P_a}$  value below 0.05 and within one standard deviation of the mean, a reasonable approximation for a low crosswind condition can be made. Therefore, in order to differentiate periods of high and low wind conditions, Fig. 7 plots the pressure drag coefficient with respect to the absolute value of the asymmetry measure, shown by the grey markers. Overall, 13 different trips, each with a unique loading configuration were analysed. A least squares quadratic line of best fit was applied to each applicable test case, with  $R^2$  values ranging from 0.695 to 0.913 (Tables 4 and 5). The dotted line are results a double-stacked container configuration with no empty slots either side (Runs D1(0), D2(0) and D3(0)). The dashed line represents a double-stacked configuration, with the instrumented container load on top and with one empty slot either side (Runs D4(1) and D5(1)). The dash-dot line represents a single-stacked train with one empty slot either side of the container (Runs S1(1), S2(1) and S3(1)) and finally the solid lines represents a single-stacked configuration where the front gap was equal to two slots or larger in size (Runs S7(2+) and S8(2+)).

Despite the position of the container from the front of the train for each configuration ranging anywhere between  $10 - 100L$  (normalised by the length of the container) for similar loading configurations, the quadratic fits remain consistent. As suggested by Quazi et al. (2020), asymmetry levels  $\leq 0.05$  were found to be reasonably consistent with nearby weather station data recording low crosswind conditions. Asymmetry levels  $\geq 0.05$  were generally found to correspond to high-wind conditions where the prevailing wind direction would result in the train experiencing a crosswind. For single-stacked configurations where there were no empty slots either side (Runs S4(0), S5(0) and

S6(0)) the magnitude of the asymmetry measure does not exceed beyond  $\sim 0.15$ . In this case the spread of data did not allow a reliable quadratic fit for the pressure coefficient to be estimated. As such in Fig. 7 the measured points are plotted in colour and not greyed out. The black markers represent numerical results processed from the work carried out by Maleki (2020) for a double-stacked 6-container consist under yawed conditions, where only the top stacked container was considered. These provide a direct comparison to the field results.

### 3.1.1. Low-wind conditions

For both single and double-stacked configurations, the data points in Fig. 8 relate the gap pressure drag coefficient as a function of the gap size,  $G$ , normalised by the width of the container, for when the asymmetry measure was  $\leq 0.05$  and within one standard deviation ( $\sigma$ ) of the mean ( $\mu$ ), corresponding to low-wind conditions. In all cases the front and base gap size are the same. Data points above this threshold ( $\mu + \sigma$ ) were considered to be head wind conditions and below this threshold ( $\mu - \sigma$ ) tail wind conditions. The “error” bars represent the range of pressure drag coefficients measured when the asymmetry level was  $\geq 0.05$  throughout the entire trip. It is evident that both the magnitude and the change in the drag coefficient with gap size are similar for both the single- and double-stacked cases, suggesting the relationship is independent of stacking type, noting that in the double-stacked configuration only the top container is considered. The highest rate of change in the drag coefficient of 0.2 per  $W$  is seen to be from a gap size of  $1.8W$  up to approximately  $4.0W$ . Once the gap size exceeded  $14.0W$  minimal increases in the pressure drag coefficient are seen.

For gap sizes  $3.37W$  (Run D1(0)) and  $3.87W$  (Run D3(0)) the loading configuration is the same, where the container is double-stacked with no empty slots either side. Hence, the difference in the gap size is only a result of the different container length immediately upstream to the instrumented container. This increase in the gap size of  $0.05W$  when referring to the work of Li et al. (2017) correlates to a 0.1 increase in the drag coefficient, which is also reflected here in the difference in the drag, 0.2 to 0.3. This suggests that when loading different length containers in the same loading configuration where the gap size lies in the high gradient region,  $1.5W - 4W$ , it can have a significant effect on the overall drag of the train.

Also included in Fig. 8 are results from Li et al. (2017) and Maleki et al. (2019) who performed wind-tunnel and numerical investigations

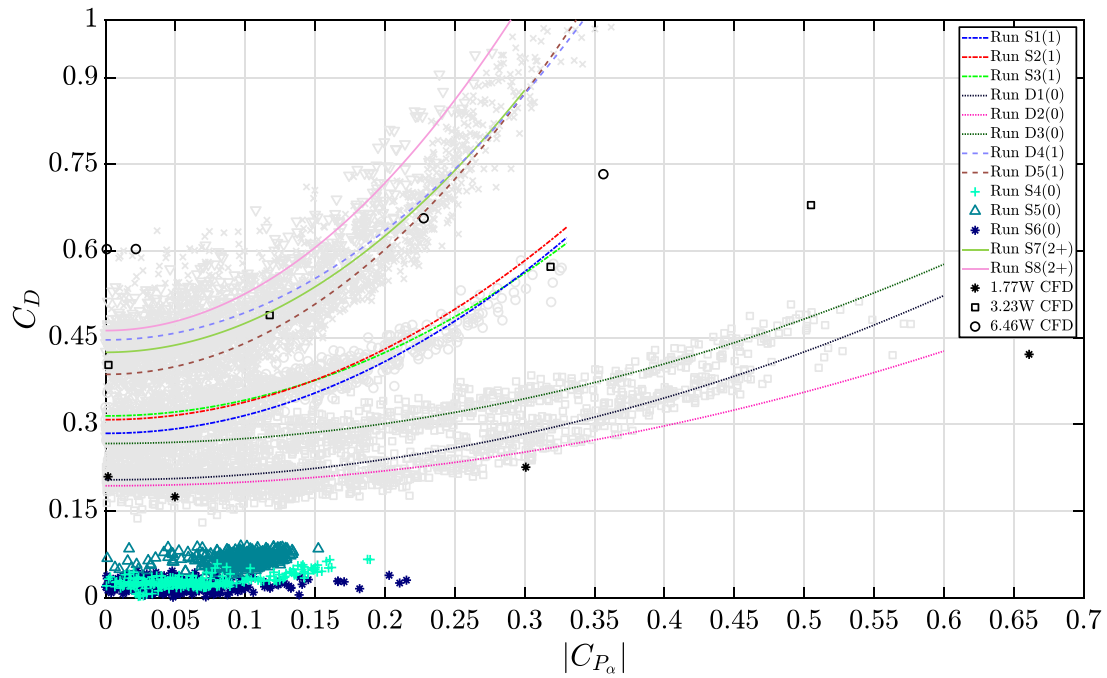


Fig. 7. Change in drag coefficient with absolute asymmetry level ( $C_p$ ) for different loading configurations. Grey markers represent the raw data with the coloured lines being the quadratic fit to each run. The coloured markers are for runs where no trend fit could be made. The black markers are from the numerical study of Maleki (2020). (For interpretation of the references to colour in this figure legend, the reader is referred to the web version of this article.)

Table 4

Statistics for the acquired pressure data for double-stacked runs along with a summary of low crosswind conditions over the length of the trip. The bracketed numbers after the title represent the number of empty slots either side of the instrumented container. Where,  $G_f$ , is front gap size normalised by the width of the container,  $P$ , is the position of container from the front of the train normalised by the length of the container and  $R^2$ , is the measure of the goodness of the fit. The subscript  $_L$  represents 'low' wind conditions.

Parameter	Run D1(0)	Run D2(0)	Run D3(0)	Run D4(1)	Run D5(1)
$G_f$ (W)	3.37	3.37	3.87	12.10	11.43
$P$ (L)	104.44	10.37	32.59	85.93	28.89
$R^2$	0.891	0.735	0.870	0.864	0.898
RMS ( $ C_{P\alpha}  \geq 0.05$ )	0.021	0.015	0.021	0.050	0.038
RMS ( $ C_{P\alpha}  \leq 0.05$ )	0.019	0.016	0.025	0.075	0.031
$\bar{C}_D$ ( $ C_{P\alpha}  \leq 0.05$ )	0.205	0.198	0.268	0.472	0.402
$\bar{T}$ ( $^{\circ}$ C)	24.2	14.8	15.4	29.9	12.4
$\bar{V}_{w_L}$ (km/h) and $\bar{\phi}_{w_L}$ ( $^{\circ}$ )	10.1 ENE	18.9 NNE	15.0 SE	29.2 WSW	7.2 SE
$\bar{V}_{T_L}$ (km/h) and $\bar{\phi}_{T_L}$ ( $^{\circ}$ )	102.2 E	108.7 E	97.5 E	102.7 W	106.1 W
$\bar{V}_{r_L}$ (km/h)	93.1	101.1	89.1	82.3	111.3
Identified wind type	Head	Cross	Head	Head	Tail
$\bar{\theta}_{yaw_L}$ ( $^{\circ}$ )	2.6	9.5	-7.7	8.3	2.6

Table 5

Statistics for the acquired pressure data for single-stacked runs along with summary of low crosswind conditions over the length of the trip, where \*, represents the RMS and  $C_D$  for the entire data set. The bracketed numbers after the title represent the number of empty slots either side of the instrumented container.

Parameter	Run S1(1)	Run S2(1)	Run S3(1)	Run S4(0)	Run S5(0)	Run S6(0)	Run S7(2+)	Run S8(2+)
$G_f$ (W)	7.24	6.74	6.87	0.31	0.31	0.31	13.57	56.57
$P$ (L)	84.44	53.33	103.70	31.70	6.15	108.89	13.85	99.26
$R^2$	0.913	0.826	0.800	-	-	-	0.695	0.855
RMS ( $ C_{P\alpha}  \geq 0.05$ )	0.019	0.019	0.020	-	-	-	0.038	0.042
RMS ( $ C_{P\alpha}  \leq 0.05$ )	0.023	0.018	0.020	0.008*	0.010*	0.011*	0.033	0.048
$C_D$ ( $ C_{P\alpha}  \leq 0.05$ )	0.292	0.316	0.321	0.029*	0.065*	0.022*	0.454	0.478
$\bar{T}$ ( $^{\circ}$ C)	22.0	14.5	15.3	5.0	13.3	23.6	18.4	10.4
$\bar{V}_{w_L}$ (km/h) and $\bar{\phi}_{w_L}$ ( $^{\circ}$ )	10.3 ESE	10.1 SSW	11.0 SW	7.4 NW	12.2 S	37.5 NW	8.2 SSW	13.4 NNE
$\bar{V}_{T_L}$ (km/h) and $\bar{\phi}_{T_L}$ ( $^{\circ}$ )	99.5 E	105.2 NW	96.8 WSW	105.1 NW	81.8 ESE	96.5 ESE	105.5 SE	108.2 NNW
$\bar{V}_{r_L}$ (km/h)	90.4	109.0	99.7	99.0	81.7	120.4	103.8	-
Identified wind type	Tail	Head	Head	Head	Cross	Tail	Cross	Head
$\bar{\theta}_{yaw_L}$ ( $^{\circ}$ )	-2.9	4.8	2.5	0.3	-8.6	6.3	-4.3	-6.1

respectively on a simplified double-stacked train consisting of 6 containers and a locomotive over a range of gap sizes. At the smallest single- and double-stacked gap sizes the field results compare well with

these studies. However, for gap sizes  $> 1.75W$  the field results are approximately 50% lower than those reported in the wind-tunnel and numerical investigations. This is in line with that found in the field

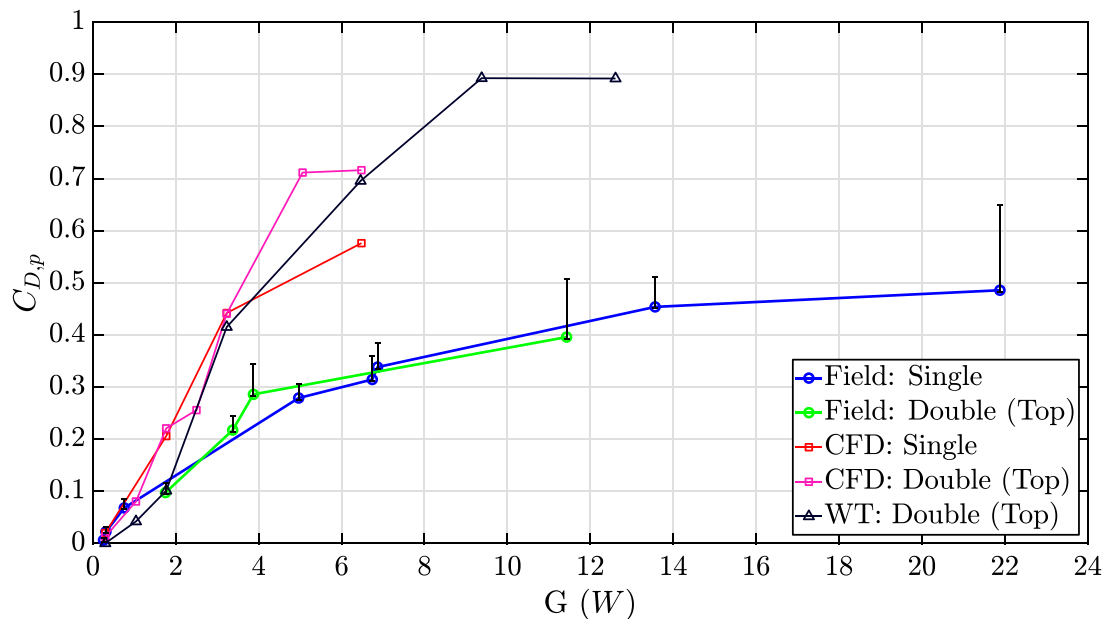


Fig. 8. Comparison of change in drag coefficient with gap size for single and double-stacked configurations between the current field study, wind-tunnel and numerical investigations of Li et al. (2017) and Maleki et al. (2017). Front and base gap sizes are the same for all cases.

study of Quazi et al. (2020) using the same setup. One of the primary differences between these studies are that the field results have been obtained at positions  $\geq 140$  m from the nose of the train, whereas the wind-tunnel and numerical studies, were carried out at distances between 46 – 75 m at full-scale. It is hypothesised that the large difference in the position along the train at which drag coefficients have been assessed, is one of the primary reasons for the difference in drag coefficients reported between the studies. This trend is also consistent during yawed conditions as can be seen in Fig. 7, where the numerical results, shown by the black markers, are 50% higher compared to equivalent full-scale gap sizes tested. This is discussed further in Section 3.2

Fig. 9 illustrates the pressure distribution contours of the front surface ( $C_p$ ) of the container for varying gap sizes for cases when the instrumented container was loaded on top of a double-stacked loading configuration for low-wind conditions. The pressure distribution was determined by interpolating between each discrete pressure tap across the surface and also by extrapolating to the outer edges of the container. The contours exhibit similar qualitative characteristics to those identified by Li et al. (2017), where low pressures are observed towards the edges as the air likely accelerates around the corner and a high stagnation pressure region exists at the centre. This is consistent over all gap sizes where only the quantitative magnitude differs between cases. In Fig. 10 for the single-stacked loading, the same general pressure distribution can be seen, however, the bottom edge of the container exhibits lower pressure than that in the double-stacked results. This can likely be attributed to the container sitting directly on the wagon, hence, the floor boundary-layer reducing the impinging wind velocity.

### 3.1.2. High crosswind conditions

Between the five different loading configurations considered in Fig. 7, presented in Section 3.1, distinct differences in the general nature of the trends can be seen for asymmetry values  $C_{p_a} \geq 0.05$ , corresponding to high crosswind conditions. For a double-stacked container with a gap size of 2 slots or larger,  $\sim 11.8W$  (D(1)), the rate of change in drag coefficient is much higher as the asymmetry level increases compared to the smaller gap size of  $\sim 3.5W$  (D(0)). This is consistent with the findings from Maleki et al. (2020), who identified in their numerical simulations that for the largest gap size tested,  $6.46W$ , a low-pressure longitudinal vortex along the roof and leeward surfaces

prevented the wake behind the container to close and bridge the gap. Hence, allowing the free stream flow to enter the gap and impinge on the front surface of the downstream container. For a gap size of  $3.23W$ , the same flow mechanism was observed, however, the effective exposed area is reduced. The resultant front pressure distributions are shown in Fig. 11 which were post-processed from the raw numerical data collected by Maleki (2020). This flow mechanism is apparent especially across gap sizes  $1.77W$  and  $3.23W$  for yaw angles  $\geq 5^\circ$ . A similar observation can be made from the field results as seen in Fig. 12, where large areas of low pressure are seen on the front surface with regions of high pressure only apparent along the windward edge. This explains the large asymmetry level magnitudes with low sensitivity to drag coefficient seen for the double-stacked container with a gap size of  $\sim 3.5W$  (D(0)).

Tables 4 and 5 summarise the statistics from the different runs. Comparing the same two double-stacked loading configurations for a  $\sim 11.8W$  (D(1)) gap size, the standard deviation is  $\sim 0.04$  whereas for the smaller double-stacked gap size it is  $\sim 0.02$ . Furthermore, for the two repeated runs at  $\sim 11.8W$  (D(1)) a relatively large offset at low asymmetry values in the drag coefficient,  $\sim 0.08$ , can be seen. This relates directly to the magnitude of the front pressure distributions seen in Figs. 9e and 9f. The finding is consistent with pressures acting on containers with larger upstream gaps being more susceptible to changes in the magnitude of head and tail-winds. It also demonstrates that only referring to the magnitude of the asymmetry measure is not sufficient to characterise the observations. For this particular case, the weather station data suggested that a consistent crosswind of around 21 km/h was present throughout the entire trip potentially leading to the observed offset. However, as the asymmetry level increases, the trend lines start to converge indicating that the crosswind component starts to become the dominant factor in the drag coefficient magnitude. A similar offset is also apparent for the smaller gap size of  $\sim 3.50W$  between runs D1(0) and D2(0) with run D3(0), however, the difference is consistent throughout the entire range of asymmetry values. Referring to Table 4 it is noted that the gap size for run D3(0) is slightly larger, at  $3.87W$  compared to  $3.37W$  for runs D1(0) and D2(0). Together coupled with a high south-easterly head-wind of 15 km/h, this may provide a reason for the offset in this particular case.

For the single-stacked case where the gap size is in between the double-stacked configurations,  $\sim 6.70W$  (S(1)), the trend for asymmetry

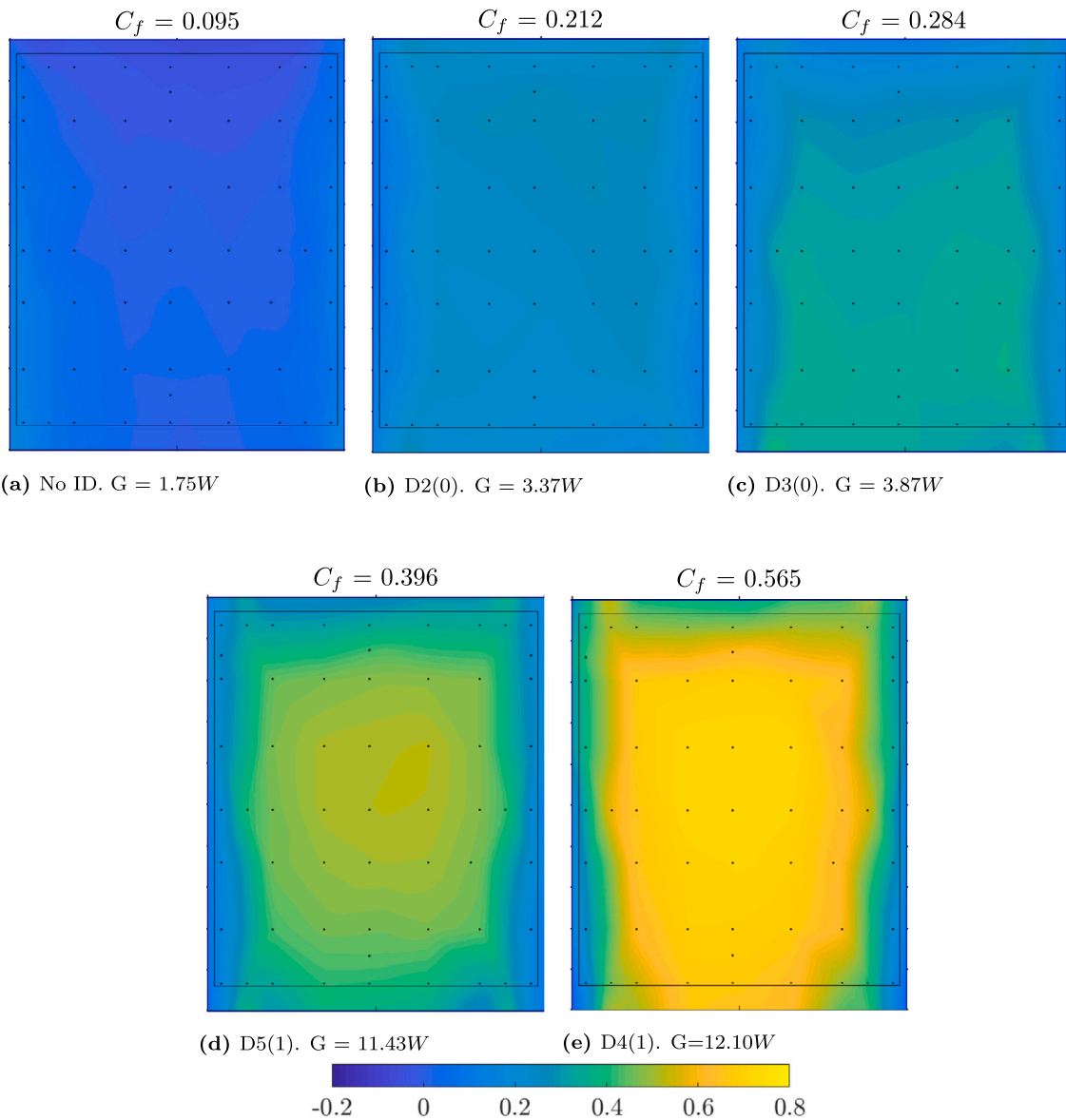


Fig. 9. Front pressure contour plots for gap sizes ( $G$ ) ranging from  $1.75W$  to  $12.10W$  for test cases when the container was positioned on top of a double-stacked loading configuration. Note, for (a) limited data was available hence no ID was assigned.

values  $\geq 0.05$  remains the same in relation to the magnitude and the rate of change of the drag coefficient. This highlights that the observed relationships are independent of whether it is single or double-stacked providing further confidence that the changes are a result of changing wind conditions and yaw angles. The same conclusion was also made from Fig. 8 for low wind conditions. Fig. 12 clearly illustrates the expected asymmetric surface pressure distribution for the four different gap size ranges tested in Fig. 7 ( $\sim 0.31W$ ,  $\sim 3.5W$ ,  $\sim 6.7W$ ,  $\geq 11.8W$ ), where the smallest gap size experiences the highest asymmetry levels and lowest drag coefficient. This observation is in line with the experimental and numerical work by Soper et al. (2015) and Maleki et al. (2020) respectively, who found similar results over different gap sizes for a given yaw angle. The governing flow physics suggests that at a smaller gap size the flow enters the gap impinging on only a small portion of the front surface and then accelerates out the opposite side creating a large region of low pressure. As the gap size increases the opposite becomes true Fig. 12.

As discussed previously, the asymmetry measure provides a proxy to estimate the wind yaw angles in lieu of a direct method for capturing the wind conditions at the exact location of the container. As such, an

attempt to build a relationship between the asymmetry measure and the wind yaw angle is shown in Fig. 13 where numerical simulations from Maleki (2020) were undertaken for a 6-container consist at 4 different gap sizes:  $0.3W$ ,  $1.77W$ ,  $3.23W$  and  $6.46W$  and 4 different yaw angles:  $0^\circ$ ,  $5^\circ$ ,  $10^\circ$ ,  $20^\circ$ . Although the data available is limited, a linear relationship can be established for gap sizes  $\geq 1.77W$  and yaw angles  $\geq 5^\circ$ . The observed relationships and associated correlation coefficients ( $R^2$ ) are,

$$\text{for } G = 1.77 W, 5 \leq \theta_{yaw} \leq 20 : \theta_{yaw} = 24.76 \cdot C_{P_\alpha} + 3.32, \text{ where } R^2 = 0.99, \tag{3}$$

$$\text{for } G = 3.23 W, 5 \leq \theta_{yaw} \leq 20 : \theta_{yaw} = 38.54 \cdot C_{P_\alpha} - 0.42, \text{ where } R^2 = 0.96, \tag{4}$$

$$\text{for } G = 6.46 W, 5 \leq \theta_{yaw} \leq 20 : \theta_{yaw} = 42.92 \cdot C_{P_\alpha} + 3.00, \text{ where } R^2 = 0.90. \tag{5}$$

From these relationships, the observed yaw angles for the pressure contour plots in Fig. 12 can be predicted for gap sizes,  $3.37W$  and

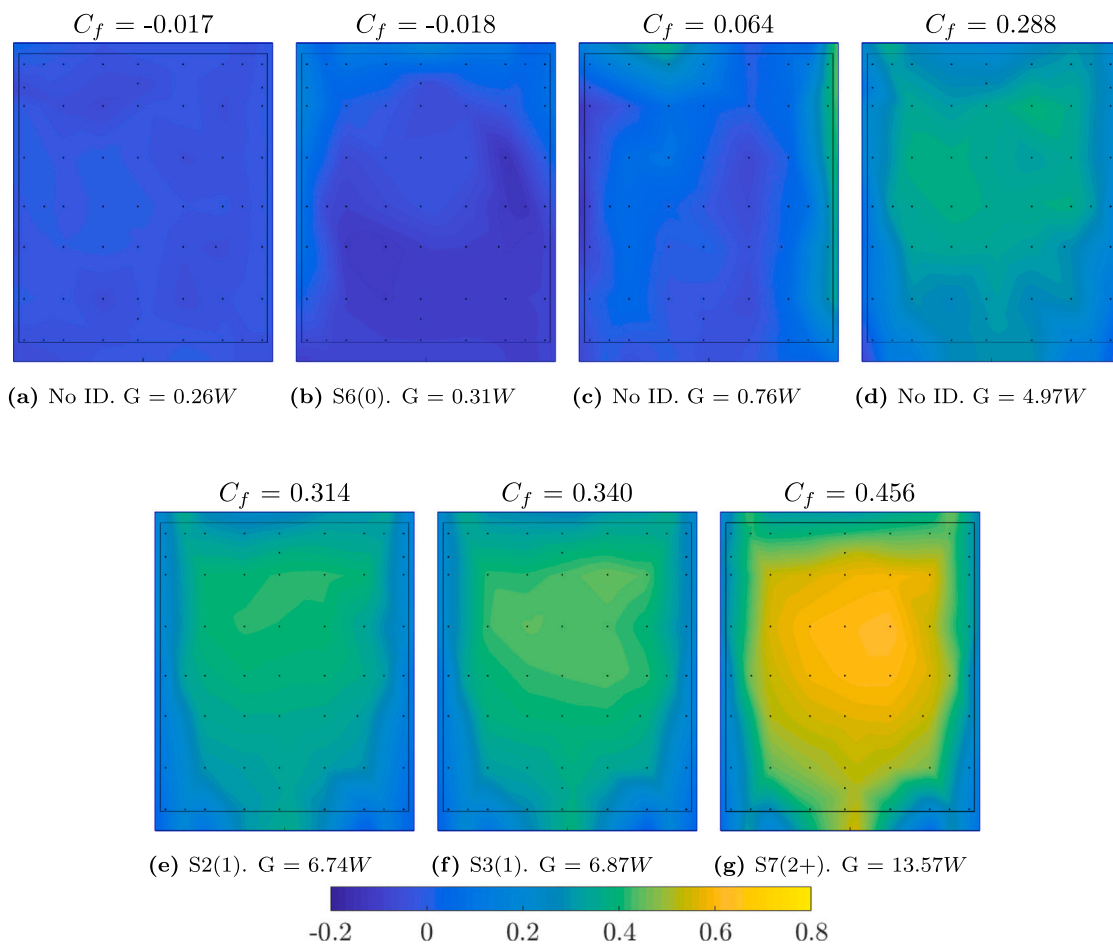


Fig. 10. Front pressure contour plots for gap sizes ( $G$ ) ranging from  $0.26W$  to  $21.88W$  for test cases when the container was in single-stacked loading configuration. Note, for (a), (c) & (d) limited data was available hence no ID was assigned.

Table 6

Estimated yaw angle determined from the previous relationships for selected runs with comparable gap sizes. Associated contour distributions are given below.

Run #	Gap size	$C_f$	$C_{p_a}$	$\theta_{yaw} (^{\circ})$
Run S5(0)	$0.31W$	0.001	0.13	–
Run D2(0)	$3.37W$	0.305	0.45	16.9
Run S2(1)	$6.74W$	0.491	0.30	15.9
Run D5(1)	$11.43W$	0.753	0.30	–

$6.74W$ , as these are close to the numerical runs that were undertaken. Table 6 highlights that the predicted yaw angles for these gap sizes respectively are  $16.9^{\circ}$  and  $15.9^{\circ}$ . The observed distributions, when compared to Fig. 11 are significantly different for similar gap size and yaw angle. In fact, the distributions more closely match the  $1.77W$  case for a similar yaw angle. This may suggest that the wake behind the container preceding the instrumented container is able to bridge the gap preventing the longitudinal vortex flowing along the roof and leeward surfaces from entering the gap. The reason for this may be due to the extreme length of freight trains, where the boundary layer around the train is more developed. This may potentially alter the acting flow physics, noting that for the numerical simulations the length of the train is very much shorter. The pressure distribution in Fig. 12(d) where the gap size is  $11.43W$  is similar to the  $6.46W$  numerical case suggesting that it takes a larger gap size for a similar pressure distribution to be observed. Hence, again this suggests the position of the container along the length of the train may have an important effect on the flow field. It is recognised that the pressure distribution may also be an artifact of the local loading configuration, nonetheless, a better

understanding of the boundary layer development around freight trains is still needed.

### 3.2. Effect of position along train

Given the extensive length a freight train can reach, an attempt has been made to better understand how the drag coefficient and surface pressure distributions change for a given gap size at different positions along the train. It is recognised that the current data set is quite limited in this regard, since at most only 3 repeated gap sizes of the same size at different positions are available. Fig. 15 plots the drag coefficient as a function of position along the train, normalised by the length of the container ( $L$ ). The drag coefficient for a given run is averaged in increments of  $0.05 C_{p_a}$  to determine if a relationship exists for both low and high crosswind conditions. It is also important to note that besides Run S5(0) all other runs are beyond  $10L$  from the front of the train, which is significantly further downstream than experimental tests in the past (Watkins et al., 1992; Gielow and Furlong, 1988; Golovanevskiy et al., 2012; Soper et al., 2014).

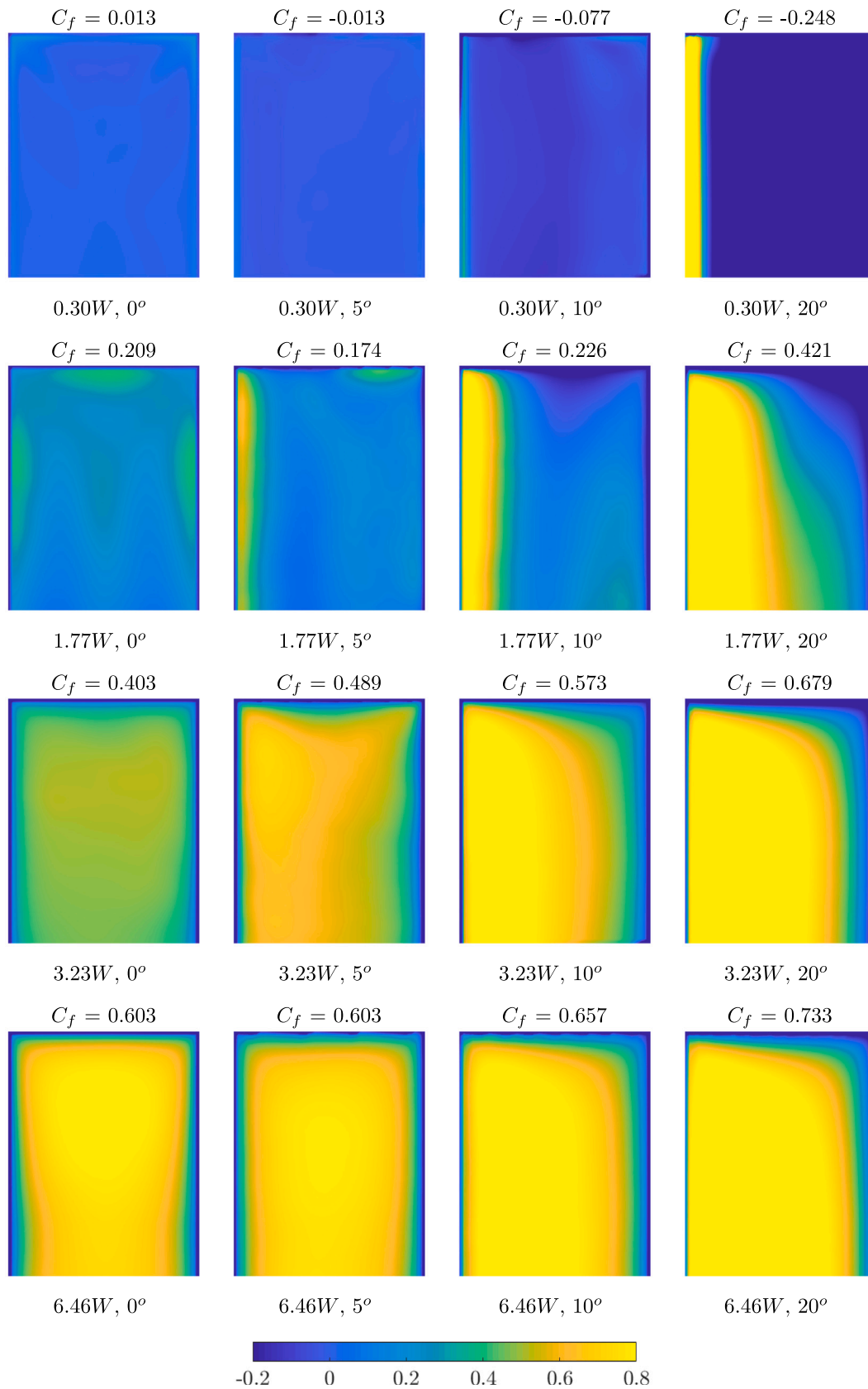


Fig. 11. Front pressure contour plots assessing different yaw angles for gap sizes ranging from 0.30W to 6.46W for test cases when the container was double-stacked on top. Results are post-processed from the work of Maleki (2020).

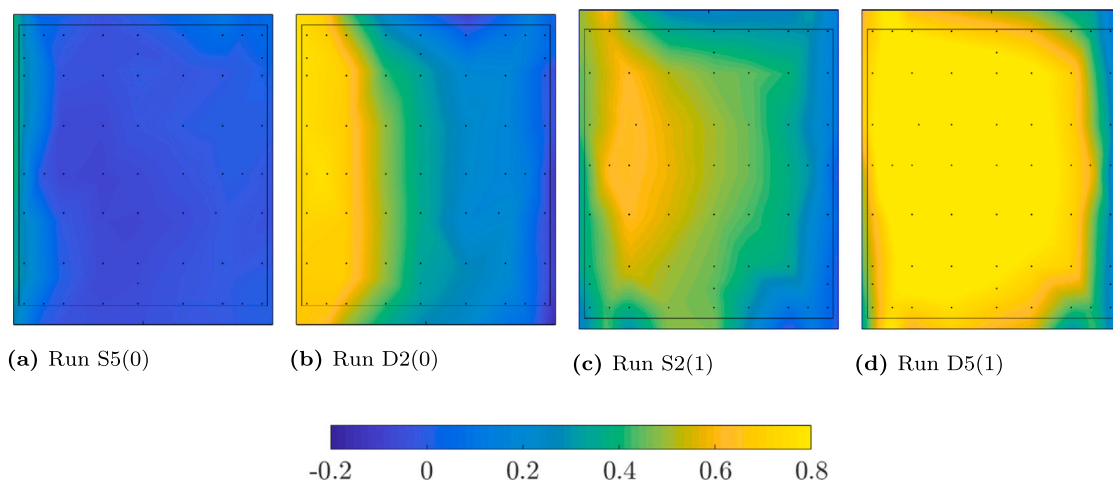


Fig. 12. Asymmetric distribution of front surface pressure contour plots for selected loading configurations. Wind direction is left to right.

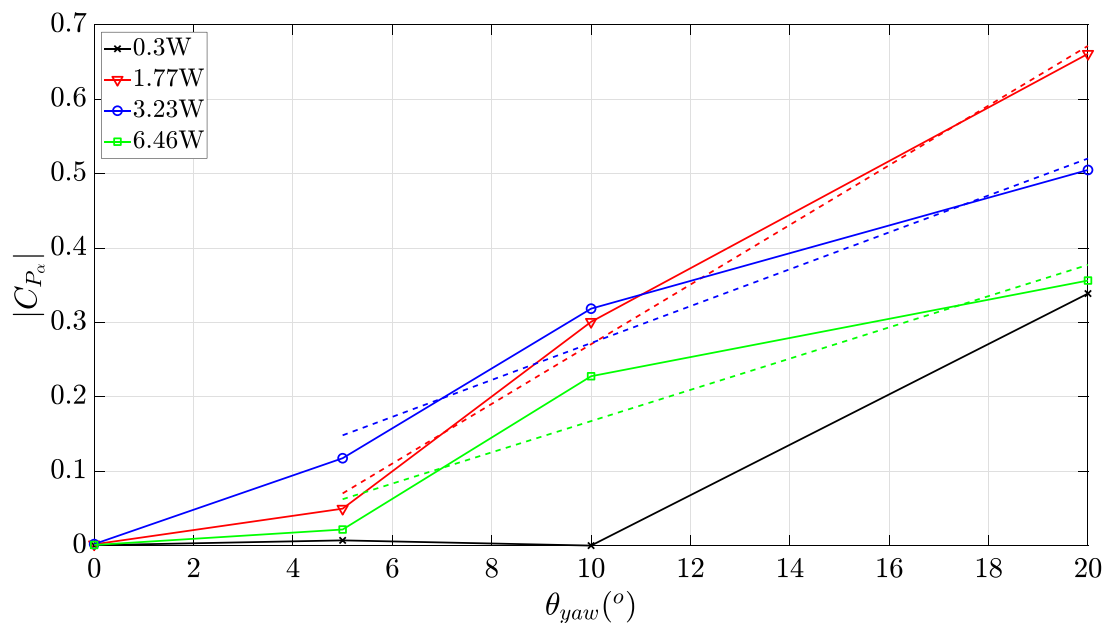


Fig. 13. Change in absolute asymmetry level with yaw angle for different gap sizes reprocessed from the numerical work of Maleki (2020).

When comparing the same loading configuration at different positions (e.g., Runs S1(1) - S3(1)), the difference in the magnitude of the low-wind condition (lowest data point for a given configuration) does not exceed 15%. However, a few exceptions apply. Run D3(0) is 70% higher than for Runs D1(0) and D2(0), even though the loading configuration is the same—the pressure distribution contours can be seen in Fig. 14. This can be attributed to the difference in the length of the upstream shipping container, and hence the gap size of  $3.37W$ , compared to  $3.87W$ , as discussed in . Furthermore, Run S5(0) is 35% higher compared to runs S4(0) and S6(0), although the gap sizes are all the same ( $0.31W$ ). This is likely due to the container being  $6L$  from the front of the train, which is understood to be within the high gradient region of drag, as the boundary layer around the train is still developing.

It was earlier shown that for low-wind conditions, the drag coefficient for all gap sizes greater than  $\geq 1.75$  was 50% lower than previous studies regardless of the position along the train. This suggests for all runs, except run S5(0), beyond a certain length, the length of the train does not correlate to an observed change in the drag coefficient. This can also be concluded from Fig. 15, and is suggested to be due to the position of the container being outside the upstream high gradient

region or due to local wind conditions having a more dominant effect. The former reasoning is evident when considering the high crosswind conditions in Fig. 15 for the larger gap size runs of S7(2+) - S8(2+) and D4(1) - D5(1). The configurations further downstream, D4(1) and S8(2+), have a larger variation in drag coefficient relative to D5(1) and S7(2+) where the average wind conditions were also higher in both runs. Hence, the expected effect associated with development of the boundary layer along the length of the train reducing the container drag coefficient at positions far from the front is not seen. In terms of field testing, further testing of containers placed in the high gradient region at the front of the train would be required to adequately determine the distance after which the container drag stabilises.

On this issue, a number of studies have attempted to investigate the effect of the length of the train. Table 7 highlights the distance from the front of the train after which the displacement boundary-layer thickness (Sterling et al., 2008; Soper et al., 2014; Bell et al., 2020; Maleki, 2020) and drag coefficient (Engdahl et al., 1987) stabilise. Engdahl et al. (1987) found that after the eighth position the drag coefficient dropped by 25% for  $0^\circ$ ,  $5^\circ$  and  $10^\circ$  yaw conditions compared to the container directly after the locomotive (second position). The curve fit for the  $0^\circ$  and  $10^\circ$  cases from this study are included in Fig. 15. The

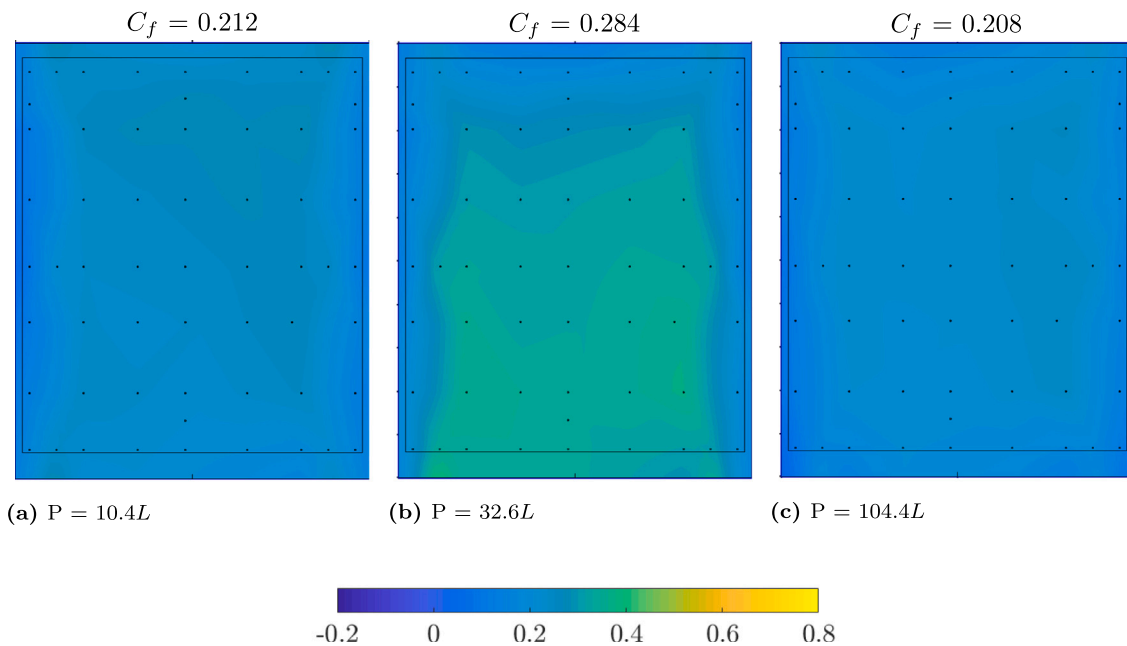


Fig. 14. Low wind double-stacked configurations with a gap size of  $\sim 3.5W$  at different positions,  $P$ , along the train normalised by the length of the container,  $L$ .

test was conducted on a full-scale open top gondola type wagons with gap sizes of  $0.3W$  either side. The open top was completely covered and the drag on the entire wagon was measured using a force balance, hence, taking into account frictional losses. This may contribute to the higher drag value compared to the similar gap size tested in this study. Through numerical modelling, Maleki (2020) quantitatively found a similar trend, where after the eighth gap size the development of the displacement boundary layer thickness stabilised. In that numerical setup the upstream gap size was  $6.47W$ , where a relaxation domain (no gaps between containers) was used to reduce the flow effects from the upstream gap, leading to a longer train being tested and a stabilisation distance of  $48.5L$ , but again noting that this corresponds to only eight gaps. Finally, in the full-scale boundary-layer characterisation of Bell et al. (2020) the stabilisation distance was found to be 200 m or at  $13.7L$  from the front of the train. Again this distance is well ahead of where the majority to containers were situated in this study, hence strengthening the case that all tests were done beyond the high gradient region.

Most previous studies, especially wind tunnel and numerical simulations, have selected a length of train model that is assumed to be representative of a significant portion of the train, away from the upstream high gradient region. It was expected that the container drag coefficient found in the current field study should be similar. However, as shown, this is not the case in low cross-winds. This suggests that in the absence of crosswinds and local effects, the drag coefficient stabilises over a much greater distance than previously thought. This is especially relevant to very long trains ( $>1$  kilometre) where the drag appears to reduce since even in the low wind cases a slight crosswind is always present. Hence, in past numerical and wind-tunnel studies (Li et al., 2017; Maleki et al., 2019), where only a parallel streamwise flow is considered, the drag coefficient may reach its constant value over much longer distances than previously expected. This highlights the importance of yawed flow over such long freight trains, which agrees with the understanding that boundary layer development for a full-scale train will be affected by a number of variables. Therefore, it will likely behave differently to that seen in simplified wind-tunnel or numerical studies.

### 3.3. Aerodynamic efficiency

From a practical point of view, a number of factors are taken into consideration when loading a freight train, however, aerodynamics

Table 7

Displacement thickness and associated stabilisation distance of the drag coefficient from the front of the train, normalised by the length of a container,  $L$ , for freight trains from various studies. \*The distance of  $48.5L$  corresponds to only 8 inter-wagon gaps noting how the simulation model was set up—see text for details.

Author	Test type	Displacement thickness $\delta$ (m)	Stabilisation distance ( $L$ )
Engdahl et al. (1987)	Full-scale	–	11.0
Sterling et al. (2008)	Full-scale	0.1 - 0.4	–
Soper et al. (2014)	Moving-model	0.6 - 1.4	6.8
Bell et al. (2020)	Full-scale	1 - 2	13.7
Maleki (2020)	Numerical	0.15 - 0.20	48.5*

is not commonly prioritised. The current work attempts to provide a better understanding of the factors affecting the gap pressure drag associated with a shipping container. Of course, sometimes practical limitations can dictate whether these factors can be manipulated. An example is (lowering) the gap spacing between two double-stacked containers. This can be limited by the wagon type used, which in all cases considered in this study was a *well-type* wagon. Well wagons are commonly seen across all Australian freight train lines but are also common in the USA, Canada, India and China. These lower the centre of gravity and also the height of the freight and hence achieve the required clearance level for tunnels (Lai et al., 2008; Upadhyay et al., 2017). However, they do so by positioning the wheels in front and behind the loading area. As a consequence, this increases the minimum attainable gap size. In the current study, the smallest gap size for a double-stacked configuration is approximately  $3.37W$  when two 48-foot containers are placed on consecutive wagons. This gap lies in the identified high gradient region, where the drag coefficient increases most rapidly with gap size and small changes can make a significant difference. The effect can be seen by considering containers of different lengths. For example, a 48-foot container followed by a 40-foot container gives a gap size of  $3.87W$  or two 40-foot containers following each other gives a gap size of  $4.37W$ . Interpolating from Fig. 8, this could lead to a 50% increase in the gap drag coefficient when compared with having two 48-foot containers next to each other. Another interesting case is having two containers of different lengths in a double-stack arrangement, i.e., the bottom container of a different length than the top container will create localised effects on the drag since the gap sizing will be different for the top and bottom containers.

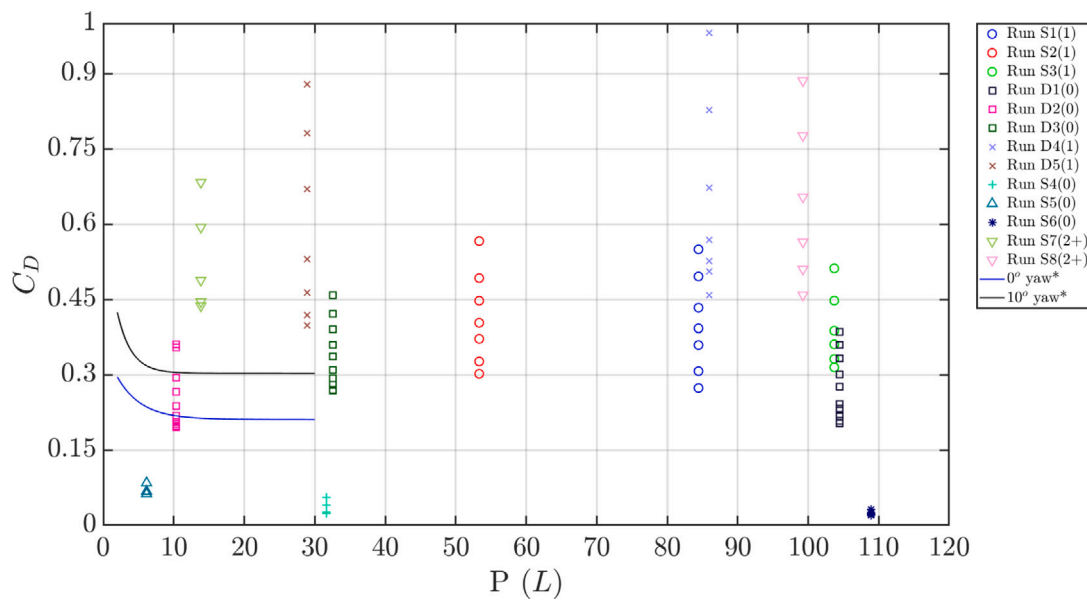


Fig. 15. Drag coefficient as a function of position along the train,  $P$ , where  $L$  is normalised by the length of the container (14.6 m). Each data point at a single position represents the average  $C_D$  over 0.05  $C_{p_e}$  increments from 0–0.5. \*Curve fit lines taken from Engdahl et al. (1987).

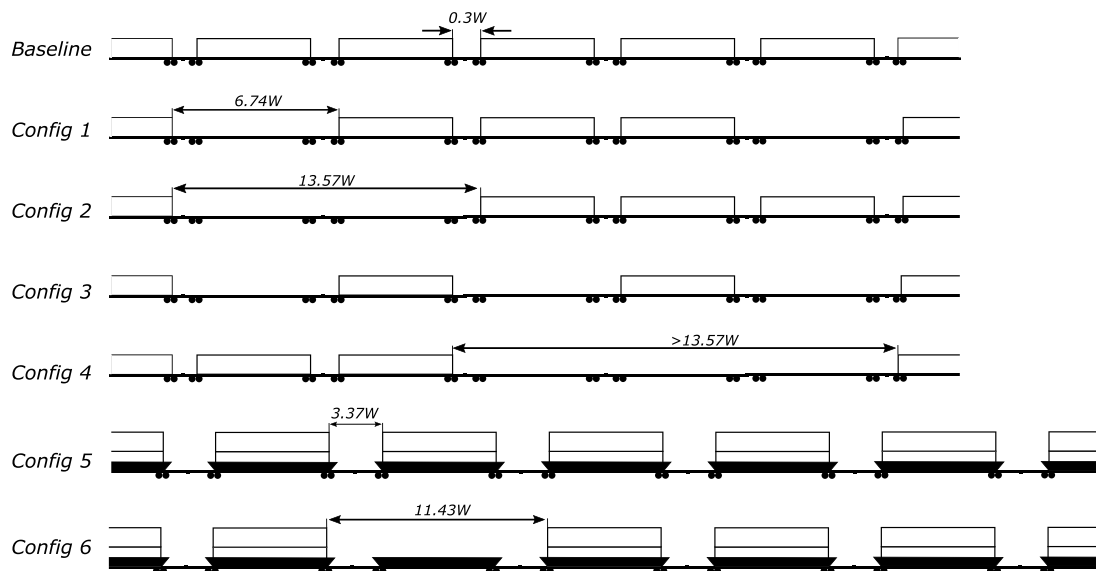


Fig. 16. Different loading configurations with various gap spacings for a set of six wagons. Total  $C_D$  and relative efficiency for each configuration is given in the table below.

To understand how different loading configurations can affect the drag coefficient, six 48-foot container slots were combined into seven different loading configurations as shown in Fig. 16. The baseline and the most aerodynamic efficient configuration is a single-stacked train with no empty slots. Table 8 corresponds to Fig. 16 and summarises the total drag coefficient and aerodynamic efficiency for each configuration. The ‘Total  $C_D$ ’ is the drag coefficient associated with the combined gap pressure drag at zero degrees yaw for each gap. It is assumed the front gap size dominates the drag coefficient as was shown in Li et al. (2017). Since the number of slots, hence the number of wagons are the same across all configurations, the wagon associated drag is assumed to be the same for all configurations where the same wagon type is used. As a coarse estimate for the additional drag associated with a well-type wagon, the drag coefficient for the bottom container in a double-stacked configuration is assumed to be the same as the top container. Although half the bottom half of the bottom container sits within the well-wagon, the well-wagon itself will experience a pressure

drag. While this may be affected by the reduced gap size between wagons compared to the containers, it seems a useful first-order estimate. Nonetheless, it is noted that the drag of a well-wagon is likely to be higher than the drag of a flat wagon, conversely, only half the number of well-wagons are required to transport an equivalent number of containers as required on flat wagons.

‘Average  $C_D$  per container’ is defined as the ratio between the ‘Total  $C_D$ ’ and the number of containers the configuration can move. ‘Relative  $C_D$ ’ and ‘Relative  $\overline{C_D}$  per container’ are the ratio of ‘Total  $C_D$ ’ and ‘Average  $C_D$  per container’, respectively, to the Baseline case. The ‘Total  $C_D$  for 10° yaw’ is also provided to estimate the change in the drag coefficient with crosswind. Here, 10 degrees was chosen since this yaw angle was simulated by Maleki (2020), hence predictions are available that define the relationship between yaw angle and drag coefficient. This was required for the 0.3W gap size since for that case yaw angle could not be predicted from asymmetry (Fig. 13). The resultant value was factored using the percentage difference between

**Table 8**

Summary of drag coefficient and aerodynamic efficiency for six wagons slots with different loading configurations. Total  $C_D$  is the drag coefficient associated with the gap pressure drag. Wind-tunnel (WT) relative  $C_D$  results are from Li et al. (2017). Average  $C_D$  per container is the ratio of the Total  $C_D$  to the number of containers.

Config #	Total $C_D$	No. of containers	Relative $C_D$	WT Relative $C_D$	Average $C_D$ per container	Relative $\overline{C_D}$ per container	Total $C_D$ ( $10^\circ$ yaw)	Relative $C_D$ ( $10^\circ$ yaw)
Baseline	0.132	6	1.000	1.000	0.022	1.000	0.264	1.000
1	0.674	4	5.106	5.04	0.169	7.682	0.850	3.220
2	0.516	4	3.909	3.28	0.129	5.864	0.676	2.561
3	0.945	3	7.159	7.07	0.315	14.318	1.143	4.337
4	0.530	3	4.015	3.09	0.177	8.046	0.676	2.561
5	2.616	12	19.818	–	0.218	9.909	2.640	13.045
6	2.536	10	19.212	–	0.254	11.546	2.460	9.318

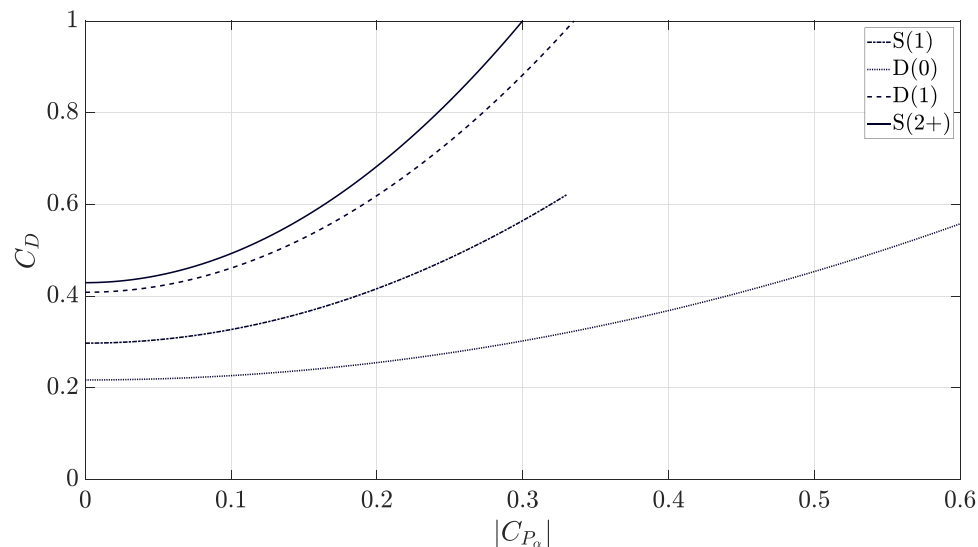


Fig. 17. Averaged drag coefficient as a function of asymmetry for the four different loading configurations. Each line type represents a different loading type.

0 and 10 degree simulations and applied to the zero degree case for the field. The largest gap size simulated by Maleki (2020) was  $6.46W$ , therefore, for field results where the gap size was larger than this, the drag coefficient was scaled to match the ratio between the drag of a  $6.46W$  gap at 0 and 10 degrees yaw. The main assumption between these derived values is that an approximate linear relationship exists, thus allowing scaling by ratios.

From the ‘Relative  $C_D$ ’, it is apparent that it is best to avoid multiple single empty slots on a single-stacked train, such as Configurations 1 and 3, when compared to Configurations 2 and 4, respectively. Hence, if empty slots are required it is best to couple two or more together in a single-stacked configuration. These results match closely with the ‘WT Relative  $C_D$ ’ values found by Li et al. (2017) for the same configuration arrangements. This suggests that, although the magnitudes are different between field and wind-tunnel studies, the relative changes remain consistent.

For Configuration 5, the ‘Relative  $C_D$ ’ is the highest of all the configurations, with it being almost 20 times worse than the baseline case. This is driven by the fact that the exposed frontal area for each gap is twice that of the single-stacked train. However, the number of containers it can carry is also twice as much, hence the question becomes whether the added capacity can compensate for the added drag. This can be evaluated by referring to the ‘Relative  $\overline{C_D}$  per container’. From this it is apparent that Configuration 5 is more aerodynamically efficient than Configuration 3; however, still considerably less efficient than the remaining single-stacked configurations. This suggests that the drag coefficient for a gap size of  $3.37W$ , which is in the high gradient region as identified in Fig. 8, is sufficiently high to prevent the added capacity providing an advantage.

Of course, aerodynamics is only one contributor to the overall resistance. The rolling resistance is the other significant contributor.

This is directly related to the number of wheels in contact with the rail. An argument can be made that since fewer double-stacked wagons are required to move the same number of containers, the rolling resistance may be less. However, a number of unknowns, including the influence of additional axle load on the double-stacked wagons and the general design differences between a flat and well-wagon (wheel shape, wheel-rail contact, bearing resistance, etc.), means further analysis would be required to evaluate if the reduced number of wagons correlate to an overall lower train resistance. This ultimately feeds into the energy consumption and hence the overall fuel efficiency. A number of studies (Lukaszewicz, 2007; Rochard and Schmid, 2000; Szanto et al., 2016) have attempted to evaluate the relative contributions to the overall resistance. These suggest that the number of axles present within the train has a larger influence on the resistance than the axle load. Assuming this holds true, it suggests that, at least in terms of rolling resistance, a double-stacked well-wagon is preferred to a single-stacked flat wagon.

From the ‘Total  $C_D$  for  $10^\circ$  yaw’ results, the drag coefficient increases with yaw angle. It is apparent that in yawed conditions, for Configurations 2 and 4, the drag coefficient is similar to Configuration 1 at zero yaw. Comparing the ‘Relative  $C_D$ ’ for 0 and 10 degrees yaw, it is evident that the aerodynamic advantage relative to the baseline configuration reduces.

The main practical implications of this work to freight train loading can be summarised as follows:

- For double-stacked configurations two or more sets of 48-foot containers should be paired by with each other. A 50% improvement in the gap  $C_D$  is seen compared to double-stacked 40-foot containers due to the reduced gap size.
- In a single-stacked configuration a single large gap, two or more empty 48-foot slots, is more efficient than having multiple empty single slots.

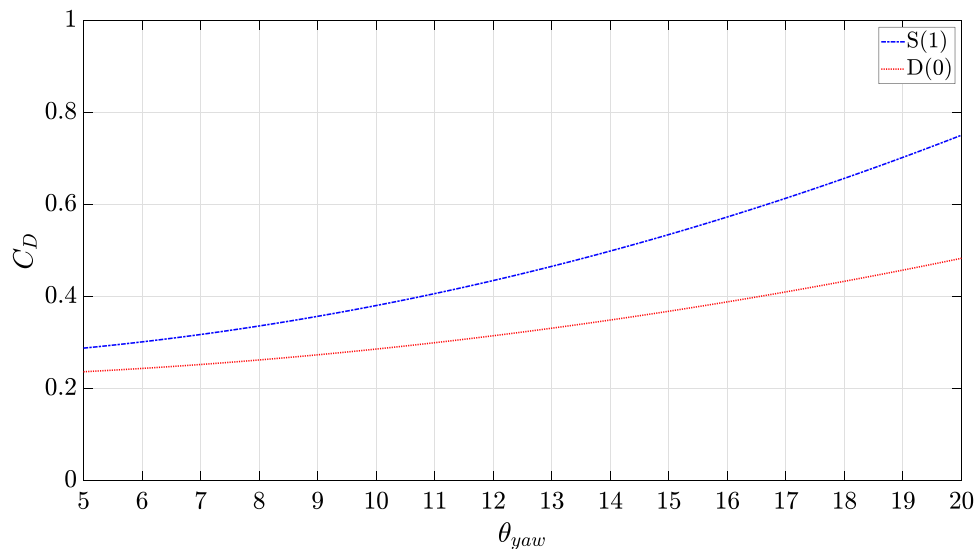


Fig. 18. Drag coefficient as a function of yaw angle derived from numerical and field-based relationships.

- Double-stacked well-wagons should not have any empty slots, since a single empty slot is less efficient than two or more single empty slots in a single-stacked configuration.
- A double-stacked well-wagon may be more energy efficient than a single-stacked flat wagon for the same number of containers.

$$\text{for } S(1) : C_D = 2.969 \cdot (C_{p_a})^2 + 0.298. \quad (6)$$

$$\text{for } D(0) : C_D = 0.946 \cdot (C_{p_a})^2 + 0.218. \quad (7)$$

$$\text{for } D(1) : C_D = 5.267 \cdot (C_{p_a})^2 + 0.409. \quad (8)$$

$$\text{for } S(2+) : C_D = 6.345 \cdot (C_{p_a})^2 + 0.430. \quad (9)$$

$$\text{for } S(1), 5 \leq \theta_{yaw} \leq 20 : C_D = 0.00125 \cdot (\theta_{yaw})^2 + 0.256. \quad (10)$$

$$\text{for } D(0), 5 \leq \theta_{yaw} \leq 20 : C_D = 0.000658 \cdot (\theta_{yaw})^2 + 0.221. \quad (11)$$

The other important factor contributing to aerodynamic performance is the effect of yaw angle on the drag coefficient. Fig. 17 plots the mean trends for four different stacking configurations considered in Fig. 7. The relationship for each trend is provided above. By substituting Eqs. (4) and (5), which are relationships derived from numerical simulation relating asymmetry to drag coefficient, into Eqs. (6) and (7), equations relating drag coefficient and yaw angle (between 5° - 20°) are derived: Eqs. (10) and (11). The resultant trends are highlighted in Fig. 18. This suggests that the drag coefficient for a gap size of 3.47W with a 11.3° yaw angle is equivalent to a gap size of 6.74W exposed to a wind yaw angle of 5°, noting that these are two different stacking types. In Maleki (2020) a 5° yaw angle for a 6.46W gap size corresponded to approximately an 8° yaw for a gap size of 3.23W.

A specific advantage the field measurements provide is a high fidelity relationship between asymmetry, a proxy for yaw angle, and the drag coefficient, where the observed variation is well approximated by a quadratic fit. The relationship between yaw and asymmetry, required to close the loop to relate drag to yaw directly, was developed from predictions from numerical modelling, which could be improved if more yaw angles were simulated. Hence, the results presented herein can also be used to better tailor which yaw angles should be prioritised when undertaking related numerical simulations or wind-tunnel experiments. In turn, this would enhance the application of this field data for quantitative drag prediction.

### 3.4. Limitations and future studies

A number of limitations exist with the current field study that have been touched on throughout the paper. One such limitation is inferring local weather and wind conditions using discrete weather stations along the path of the train. Placing a thermo-couple inside the container would not be representative of the external conditions, while placing it on the outside surface would be affected by the conduction of the metal surface. Similarly, mounting a pitot-static tube to attain static pressure was not possible due to regulations governing extrusions extending outside the container.

However, in terms of the data acquired, this study provided a good basis for analysing the effect of different wind environments for a given gap size given the long duration of a single trip. Theoretically, to build a better understanding of the effect of train length, multiple shorter trips with the instrumented container placed at different positions may have been a more suitable approach to attain more data points. As for the pressure distribution contours, the base pressure readings were very low relative to past studies and towards the noise floor of the pressure sensors and hence could not be confidently distinguished for each run. This may be reflective of the difficulty of obtaining full-scale wake measurements where the flow is highly separated.

The need to use the asymmetry of the front pressure distribution to estimate the wind yaw angle given the lack of a direct method has a number of limitations. Yaw angle is based on the train velocity and the wind velocity hence is independent of any pressure measurements. However, when inferring yaw angle from the asymmetry level, the observed asymmetry can be a function of the gap size, the local arrangement of containers and the surrounding topology. Further to this, the wind speed and direction were not well defined with the best estimates taken from the closest weather stations. In terms of the test setup itself, the use of LiDAR sensors and thermal cameras, as done recently by Bell et al. (2022), can provide added fidelity relating to the surrounding topology along the train line to better characterise the difference seen in the pressure measurements. Furthermore, additional pressure taps on the side and roof of the container would provide a better approximation of the side wind and enable direct correlations to wind-tunnel and numerical studies. Until a method is developed to measure the wind velocity, which also satisfies the freight operator, the method applied in this current work provides a basis for further work and comparisons with field-based data.

From an aerodynamic efficiency modelling viewpoint, it is apparent that a gap exists in assessing the pressure drag associated with a

container loaded on the bottom of a double-stacked configuration in a well-type wagon and also the drag associated with the wagon itself. By understanding how these contribute to the drag coefficient of the given gap size, a more accurate assessment can be made between double-stacked and single-stacked configurations with different wagon types.

#### 4. Conclusion

The present work extends the work carried out by Quazi et al. (2020) to cover a wide range of different loading configurations. These are analysed with the aim of furthering our understanding of how the gap size, loading type, wind conditions, and position along the train affect the gap pressure drag coefficient, and front and base pressure distributions. Under low crosswind conditions, defined in the current study by an observed asymmetry level on the front surface  $\leq 0.05$ , the magnitude of the gap pressure drag coefficient is 50% lower than that of previous reduced-scale experimental and numerical studies. This surprising finding highlights the complexity of real-world operation, and its significant effect on aerodynamic characteristics.

For high crosswind, the asymmetry measure varies with drag coefficient in an approximately quadratic manner, with increasing gap size resulting in a higher rate of change in the asymmetry level. This formed a proxy to estimate the wind yaw angle. A relationship between the asymmetry measure and yaw angle was developed from previous numerical simulations to provide a predicted yaw angle. Using this relationship, the front surface pressure distributions between numerical simulations and full-scale testing were compared. It suggested that distributions were similar when comparing larger full-scale gap sizes to smaller numerical gap sizes. In turn, this suggested that the flow physics was affected by position on the container along the length of the train where the interaction of the longitudinal vortex, closure of the wake and the boundary layer around the train needs to be better understood and characterised.

In all loading cases, the crosswind component becomes the dominant factor with asymmetry level. This is evident as the difference in the drag coefficient decreases between different runs with the same loading configuration, since the head and tail wind components have less effect. Furthermore, the trends were found to be independent of stacking type, whether single or double-stacked where only the top container was considered. The pressure contour distributions for the low-wind cases were reflective of the observed drag coefficient trends which match those found in previous publications.

For the current data-set, the test container was positioned beyond the supposed high gradient region for the drag coefficient, except for a single run. This is the region where the drag coefficient drops significantly before stabilising following the impingement of the air on the front locomotive. This may explain the similarity between in drag coefficient values regardless of the position of the container along the length of the train for the same loading configuration. Any differences that were seen could be directly attributed to differences in gap size or local wind conditions during the run. However, it highlights the importance crosswinds play in the stabilisation of the drag coefficient over the length of the train.

It was concluded that further runs would be required to determine the exact position after which the container drag coefficient stabilises to a value representative for the majority of the train. It was also shown that in the real world for a double-stacked loading configuration with no empty slots either side, the length of the container can cause a slight difference in gap sizes, which can have a significant effect on the container drag coefficient, in turn contributing to the overall freight train aerodynamic drag. If an empty slot is required within a train, it is best to avoid multiple single empty 48-foot slots. Coupling two or more empty slots to have a single larger gap is preferable. Finally, when considering the overall train resistance the higher capacity of a double-stacked configuration may be more efficient given that fewer wagons are required to move the same number of containers compared to a single-stacked configuration even though aerodynamically a single-stacked train is still the most efficient.

#### CRediT authorship contribution statement

**Ariq Quazi:** Conceptualization, Methodology, Software, Validation, Formal analysis, Investigation, Data curation, Writing – original draft, Visualization, Project administration. **Timothy Crouch:** Conceptualization, Methodology, Writing – review & editing, Supervision, Project administration. **James Bell:** Conceptualization, Methodology, Software, Validation, Writing – review & editing, Project administration, Funding acquisition. **Tony McGreevy:** Resources, Funding acquisition. **Mark C. Thompson:** Conceptualization, Supervision, Writing – review & editing, Funding acquisition. **David Burton:** Conceptualization, Methodology, Supervision, Writing – review & editing, Resources, Project administration, Funding acquisition.

#### Declaration of competing interest

The authors declare that they have no known competing financial interests or personal relationships that could have appeared to influence the work reported in this paper.

#### Data availability

Data will be made available on request.

#### Acknowledgements

This research was supported through Pacific National and the Australian Research Council's Linkage Project funding scheme, under project number LP13100953.

#### References

- Beagles, A.E., Fletcher, D.I., 2013. The aerodynamics of freight: Approaches to save fuel by optimising the utilisation of container trains. *Proc. Inst. Mech. Eng. F* 227 (6), 635–643.
- Bell, J., Burton, D., Thompson, M., 2020. The boundary-layer characteristics and unsteady flow topology of full-scale operational inter-modal freight trains. *J. Wind Eng. Ind. Aerodyn.* 201, 104164.
- Bell, J., Werner, F., Marian, B., Henning, A., 2022. Full-scale aerodynamic measurements on-board a freight train using the DLR FR8-LAB. In: 13th World Congress on Railway Research. pp. 1–7.
- Davis, W.J., 1926. *The Tractive Resistance of Electric Locomotives and Cars*. General Electric.
- Engdahl, R., Gielow, R., Paul, J., 1987. Train resistance-aerodynamics: Volume I of II. Intermodal car application. In: *Railroad Energy Technology Conference II* (1986).
- Flynn, D., Hemida, H., Baker, C., 2016. On the effect of crosswinds on the slipstream of a freight train and associated effects. *J. Wind Eng. Ind. Aerodyn.* 156, 14–28.
- Gallagher, M., Morden, J., Baker, C., Soper, D., Quinn, A., Hemida, H., Sterling, M., 2018. Trains in crosswinds—comparison of full-scale on-train measurements, physical model tests and CFD calculations. *J. Wind Eng. Ind. Aerodyn.* 175, 428–444.
- Giappino, S., Melzi, S., Tomasini, G., 2018. High-speed freight trains for intermodal transportation: Wind tunnel study on the aerodynamic coefficients of container wagons. *J. Wind Eng. Ind. Aerodyn.* 175, 111–119.
- Gielow, M., Furlong, C., 1988. *Results Of Wind tunnel and Full-Scale Tests Conducted from 1983 to 1987 in support of the Association Of American Railroads' train Energy Program*. Technical Report.
- Golovanevskiy, V.A., Chmovzh, V.V., Girka, Y.V., 2012. On the optimal model configuration for aerodynamic modeling of open cargo railway train. *J. Wind Eng. Ind. Aerodyn.* 107–108, 131–139.
- Lai, Y.-C., Barkan, C.P., 2005. Options for improving the energy efficiency of intermodal freight trains. *Transp. Res. Rec.* 1916 (1), 47–55.
- Lai, Y.-C., Barkan, C.P., Önal, H., 2008. Optimizing the aerodynamic efficiency of intermodal freight trains. *Transp. Res. E* 44 (5), 820–834.
- Li, C., Burton, D., Kost, M., Sheridan, J., Thompson, M.C., 2017. Flow topology of a container train wagon subjected to varying local loading configurations. *J. Wind Eng. Ind. Aerodyn.* 169, 12–29.
- Li, C., Kost, M., Burton, D., Sheridan, J., Thompson, M.C., 2015. Wind tunnel investigation of a double stacked wagon in free-stream. In: *ASME/JSMSE/JSME 2015 Joint Fluids Engineering Conference*. American Society of Mechanical Engineers Digital Collection.
- Lukasiewicz, P., 2007. Running resistance - Results and analysis of full-scale tests with passenger and freight trains in Sweden. *Proc. Inst. Mech. Eng. F* 221 (2), 183–193.

- Maleki, S., 2020. Numerical Investigations into the Aerodynamics of Freight Trains (Ph.D. thesis).
- Maleki, S., Burton, D., Thompson, M.C., 2017. Assessment of various turbulence models (ELES, SAS, URANS and RANS) for predicting the aerodynamics of freight train container wagons. *J. Wind Eng. Ind. Aerodyn.* 170, 68–80.
- Maleki, S., Burton, D., Thompson, M.C., 2019. Flow structure between freight train containers with implications for aerodynamic drag. *J. Wind Eng. Ind. Aerodyn.* 188, 194–206.
- Maleki, S., Burton, D., Thompson, M.C., 2020. On the flow past and forces on double-stacked wagons within a freight train under cross-wind. *J. Wind Eng. Ind. Aerodyn.* in print.
- Östh, J., Krajnović, S., 2014. A study of the aerodynamics of a generic container freight wagon using Large-Eddy simulation. *J. Fluids Struct.* 44, 31–51.
- Quazi, A., Crouch, T., Bell, J., McGreevy, T., Thompson, M.C., Burton, D., 2020. A field study on the aerodynamics of freight trains. *J. Wind Eng. Ind. Aerodyn.* 209, 104463.
- Quinn, A., Sterling, M., Robertson, A., Baker, C., 2007. An investigation of the wind-induced rolling moment on a commercial vehicle in the atmospheric boundary layer. *Proc. Inst. Mech. Eng. D* 221 (11), 1367–1379.
- Richardson, G., Hoxey, R., Robertson, A., Short, J., 1997. The Silsoe Structures Building: Comparisons of pressures measured at full scale and in two wind tunnels. *J. Wind Eng. Ind. Aerodyn.* 72, 187–197.
- Rochard, B.P., Schmid, F., 2000. A review of methods to measure and calculate train resistances. *Proc. Inst. Mech. Eng. F* 214 (4), 185–199.
- Soper, D., Baker, C., 2020. A full-scale experimental investigation of passenger and freight train aerodynamics. *Proc. Inst. Mech. Eng. F* 234 (5), 482–497.
- Soper, D., Baker, C., Sterling, M., 2014. Experimental investigation of the slipstream development around a container freight train using a moving model facility. *J. Wind Eng. Ind. Aerodyn.* 135, 105–117.
- Soper, D., Baker, C., Sterling, M., 2015. An experimental investigation to assess the influence of container loading configuration on the effects of a crosswind on a container freight train. *J. Wind Eng. Ind. Aerodyn.* 145, 304–317.
- Sterling, M., Baker, C.J., Jordan, S.C., Johnson, T., 2008. A study of the slipstreams of high-speed passenger trains and freight trains. *Proc. Inst. Mech. Eng. F* 222 (2), 177–193.
- Surry, D., 1991. Pressure measurements on the Texas Tech Building: Wind tunnel measurements and comparisons with full scale. *J. Wind Eng. Ind. Aerodyn.* 38 (2–3), 235–247.
- Szanto, F., et al., 2016. Rolling resistance revisited. In: CORE 2016: Maintaining the Momentum. Railway Technical Society of Australasia, p. 628.
- Taylor, Z.J., Palombi, E., Gurka, R., Kopp, G.A., 2011. Features of the turbulent flow around symmetric elongated bluff bodies. *J. Fluids Struct.* 27 (2), 250–265.
- Upadhyay, A., Gu, W., Bolia, N., 2017. Optimal loading of double-stack container trains. *Transp. Res. E* 107, 1–22.
- Uystepuyst, D., Krajnović, S., 2013. LES of the flow around several cuboids in a row. *Int. J. Heat Fluid Flow* 44, 414–424.
- Watkins, S., Saunders, J., Kumar, H., 1992. Aerodynamic drag reduction of goods trains. *J. Wind Eng. Ind. Aerodyn.* 40 (2), 147–178.